



An elastoviscoplastic model for porous single crystals at finite strains and its assessment based on unit cell simulations



Chao Ling ^{a, b}, Jacques Besson ^b, Samuel Forest ^{b, *}, Benoît Tanguy ^a,
Felix Latourte ^c, Elodie Bosso ^c

^a CEA, Université de Paris–Saclay, DEN, Laboratoire de Comportement Mécanique des Matériaux Irradiés, 91191 Gif-sur-Yvette, France

^b MINES ParisTech, PSL Research University, MAT – Centre des matériaux, CNRS UMR 7633, BP 87, 91003 Evry, France

^c EDF R&D, MMC, Site des Renardières, 77818 Moret-sur-Loing Cedex, France

ARTICLE INFO

Article history:

Received 21 January 2016

Received in revised form 29 April 2016

Available online 20 May 2016

Keywords:

A. Ductility

A. Fracture mechanisms

B. Crystal plasticity

B. Porous material

B. Finite strain

ABSTRACT

An elastoviscoplastic model is formulated at finite strains for porous single crystals. The model extends the yield function developed by Han et al. (2013) for porous single crystals at infinitesimal strains to finite strains, incorporating the evolution of void volume fraction and strain hardening of single crystal matrix. The model is assessed through three-dimensional unit cell finite element simulations based on periodic homogenisation and loading paths with prescribed constant stress triaxiality. The unit cell simulations are performed for face-centered cubic crystals with various crystallographic orientations, stress triaxialities and initial void volume fractions, showing the competitive influence of the stress triaxiality and the crystallographic orientation on the effective behaviour and the void volume evolution. The proposed model captures the hierarchy of porous single crystal responses with respect to crystal orientation and void volume fraction. It represents a remarkable compromise between description of unit cell behaviour and tractability in the computation of structural components.

© 2016 Elsevier Ltd. All rights reserved.

1. Introduction

Void nucleation, growth and coalescence are known as the main mechanisms of ductile fracture in crystalline metals and alloys. Numerous studies have been carried out in the last decades to understand, simulate and model these phenomena in polycrystals. Readers are referred to the reviews of Besson (2010) and of Benzerga and Leblond (2010) for more details. In comparison, less effort has been devoted to investigating the process of void growth and coalescence in single crystals. Experiments by Crépin et al. (1996) showed that the anisotropy of single crystal behaviour can induce polygonal void shape and high void growth rates in zirconium single crystals. Srivastava et al. (2012) have shown that void evolution have a significant influence on the creep fracture in Ni-based single-crystal superalloys. Development of model for porous single crystals is of interest for engineering applications, e.g., to study the ductility of stainless steels (304/316 series) used for core internals of Pressurised Water Reactor nuclear power plants or the lifetime prediction of Ni-based single crystal superalloys used in turbo-engine components.

Various methods are used to study void growth and coalescence in single crystals as well as the effective behaviour of porous single crystals. At small scale, discrete dislocation dynamics (DDD) and molecular dynamics (MD) are adequate. It has been shown by Segurado and Llorca (2010) through DDD and by Farrissey et al. (2000) and Zhao et al. (2009) through MD that

* Corresponding author.

E-mail addresses: samuel.forest@ensmp.fr, samuel.forest@mat.ensmp.fr (S. Forest).

the crystallographic orientation has a significant effect on overall mechanical behaviour (yield strength, strain hardening, etc.) and void growth rate of porous single crystals under uniaxial tension.

Unit cell (UC) methodology based on finite element (FE) simulations is another tool well suited to the mechanical calculation of porous single crystals. O'Regan et al. (1997) investigated plane strain cases and showed that initial void volume fraction has a significant effect on the peak of overall stress and that more compact void arrangement leads to softer material. Orsini and Zikry (2001); Shanthraj and Zikry (2012) studied the influence of void distribution and spacing between voids under uniaxial tension loading. They reported that material fails either by void growth and coalescence or by shear localisation and that failure mechanism is directly related to void arrangement. Gan et al. (2006) simulated the stress, strain and lattice rotation fields around a cylindrical void in Face-Centered Cubic (FCC) crystals. They reported good agreement between the results of simulations, experimental results and analytical results obtained by anisotropic slip line theory in the work of Kysar et al. (2005). Yerra et al. (2010) studied the effect of crystallographic orientation, stress triaxiality and strain hardening of the matrix on void growth and coalescence in Body Centered Cubic (BCC) single crystals using three-dimensional (3D) unit cell. They showed that stress triaxiality and crystallographic orientation have a coupled effect on the void evolution. For low stress triaxiality, void shape evolution, void growth rate and strain at the onset of coalescence are mainly determined by crystallographic orientations. At high stress triaxialities, only void growth rate depends on crystallographic orientation. Ha and Kim (2010) performed a similar study in FCC single crystals and obtained results consistent with Yerra et al. (2010) about the effects of crystallographic orientation and stress triaxiality on void evolution. They also highlighted that the void growth rate increases and the effect of orientation becomes more significant when the initial void volume fraction decreases. They do not resort to periodic boundary conditions in their simulations and consider instead planar lateral surfaces. The validity of their results is therefore limited to highly symmetric orientations. Han et al. (2013) carried out limit analysis for FCC single crystals with an initially spherical void and different crystallographic orientations by taking into account various stress triaxialities and initial void fractions, allowing to assess a yield function. Srivastava and Needleman (2013) studied the effect of Lode parameter on the evolution of a initially spherical void in FCC single crystals under creep loading. They demonstrated that in the region of low stress triaxiality, the evolution of void fraction and void shape depend on Lode parameter for symmetric crystallographic orientation (001). In addition, a more recent paper of Srivastava and Needleman (2015) also shows that for asymmetric crystallographic orientations, the effect of Lode parameter can be significant even at relatively high stress triaxiality. Mbiakop et al. (2015b) dealt with cylindrical voids with elliptical cross-section in single crystals with arbitrary number of slip systems. They showed that the effective response of single crystals with elliptical voids is softer than those with circular voids. Furthermore, they found that porous single crystals exhibit quasi-incompressible response when only one or two slip systems are activated in the matrix. The mentioned works resort to the finite element method at finite deformation but FFT-based method was also recently applied to void growth in polycrystalline aggregates (Lebensohn et al., 2013).

In the past few years, an increasing number of studies have been devoted to the development of models describing the overall behaviour of porous single crystals. A first yield function was derived by Han et al. (2013) based on a variational homogenisation method (see DeBotton and Castaneda (1995)). The explicit yield potential proposed for porous single crystals accurately represents the limit analysis results. Based on the unit cell calculations of Han et al. (2013), another model was developed by Paux et al. (2015) using a regularised form of the Schmid law and limit-analysis calculation. More recently, a two-dimensional model accounting for elliptical void shape was developed by Mbiakop et al. (2015b) following the variational method of Danas and Aravas (2012) and it was then extended to three-dimension for single crystals with ellipsoidal voids in the work of Mbiakop et al. (2015a). Based on a variational homogenisation method, a quasi-explicit yield potential suitable for small strain applications was derived. However, to the authors' knowledge, there is currently no model for porous single crystals at finite strains, which is able to describe the void evolution up to coalescence and which is simple enough for finite element implementation in order to carry out structural computations.

The aim of this work is to propose a finite deformation elastoviscoplastic constitutive model for porous single crystals that can be used in structural computations. It should incorporate the strain hardening of the matrix and be able to predict, at least qualitatively, the influence of crystallographic orientation on the stress strain response and the void growth. The proposed model is assessed using 3D FE unit cell simulations based on computational periodic homogenisation under prescribed stress triaxiality. The present work also brings new information for highly non-symmetric orientations like [120] and $\bar{1}25$ including void growth rate and void shape evolution. These non-symmetric orientations are essential to assess the validity and see the limitations of any such model, since they will be frequently encountered in practice. The applicability of the model to structural computations is finally assessed by the simulation of the tearing of a single crystal notched specimen.

The paper is organised as follows. The formulation of the porous single crystal model is presented in Section 2. Section 3 describes the FE formulation for the unit cell simulations with prescribed stress triaxiality and periodic boundary conditions. The main results of unit cell simulations concerning the influence of crystallographic orientation are given in Section 4. The assessment of the porous single crystal model is presented in Section 5. Examples of simulations using the porous single crystal model are given in Section 6 followed by conclusions in Section 7.

2. Proposed model for single crystals

A unified formulation at finite strains is proposed for void-free and porous single crystals in this part. The formulation is first presented for void-free single crystals, and then for porous single crystals by emphasizing the difference compared to the former one.

2.1. Void-free single crystals

2.1.1. Kinematics

For void-free single crystals, a lattice orientation is attributed to each material point. The existence of directors associated with lattice orientation allows for the definition of a unique isoclinic intermediate local configuration C_i , as recommended by Mandel (1973). This ensures the uniqueness of the multiplicative decomposition of the deformation gradient $\tilde{\mathbf{F}}$ adopted within the finite strain framework:

$$\tilde{\mathbf{F}} = \tilde{\mathbf{E}} \cdot \tilde{\mathbf{P}}, \quad (1)$$

with the elastic part $\tilde{\mathbf{E}}$ and the plastic part $\tilde{\mathbf{P}}$ of the deformation gradient $\tilde{\mathbf{F}}$. The crystal orientation is the same in the initial local configuration C_0 and the intermediate local configuration C_i . The determinants of $\tilde{\mathbf{F}}$, $\tilde{\mathbf{E}}$ and $\tilde{\mathbf{P}}$ describe the change of volume and of density of a material point:

$$J = \det \tilde{\mathbf{F}} = \frac{V}{V_0} = \frac{\rho_0}{\rho}, \quad (2)$$

$$J_e = \det \tilde{\mathbf{E}} = \frac{V}{V_i} = \frac{\rho_i}{\rho}, \quad (3)$$

$$J_p = \det \tilde{\mathbf{P}} = \frac{V_i}{V_0} = \frac{\rho_0}{\rho_i}, \quad (4)$$

where V_0 , V_i and V denote the volume at the reference configuration C_0 , the intermediate configuration C_i and the current configuration C ; ρ_0 , ρ_i and ρ represent the density at the reference configuration C_0 , the intermediate configuration C_i and the current configuration C . Note that $J_p = 1$ due to the incompressible plasticity of void-free single crystals undergoing plastic slip.

The velocity gradient $\tilde{\mathbf{L}}$ can be expressed as

$$\tilde{\mathbf{L}} = \dot{\tilde{\mathbf{F}}} \cdot \tilde{\mathbf{F}}^{-1} = \tilde{\mathbf{L}}^e + \tilde{\mathbf{E}} \cdot \tilde{\mathbf{L}}^p \cdot \tilde{\mathbf{E}}^{-1}, \quad (5)$$

with the elastic part of the velocity gradient $\tilde{\mathbf{L}}^e$ in the current configuration C

$$\tilde{\mathbf{L}}^e = \dot{\tilde{\mathbf{E}}} \cdot \tilde{\mathbf{E}}^{-1}, \quad (6)$$

and the plastic part of the velocity gradient $\tilde{\mathbf{L}}^p$ in the intermediate configuration C_i

$$\tilde{\mathbf{L}}^p = \dot{\tilde{\mathbf{P}}} \cdot \tilde{\mathbf{P}}^{-1}. \quad (7)$$

2.1.2. Definition of stresses

According to the approach of Mandel (1973) (see also (Sabnis et al., 2012, 2013)), stress tensors are defined as follows.

The second Piola-Kirchhoff stress tensor $\tilde{\mathbf{\Pi}}^e$, defined with respect to the intermediate configuration C_i , is given by

$$\tilde{\mathbf{\Pi}}^e = J_e \tilde{\mathbf{E}}^{-1} \cdot \tilde{\boldsymbol{\sigma}} \cdot \tilde{\mathbf{E}}^{-T}, \quad (8)$$

where $\tilde{\boldsymbol{\sigma}}$ is the Cauchy stress defined in the current configuration C .

The elastic Green-Lagrange strain tensor $\tilde{\mathbf{E}}_{GL}^e$ is defined as

$$\tilde{\mathbf{E}}_{GL}^e = \frac{1}{2} \left(\tilde{\mathbf{E}}^T \cdot \tilde{\mathbf{E}} - \mathbf{1} \right). \quad (9)$$

$\tilde{\mathbf{\Pi}}^e$ is related to $\tilde{\mathbf{E}}_{GL}^e$ by the elasticity law:

$$\tilde{\mathbf{\Pi}}^e = \tilde{\mathbf{C}} : \tilde{\mathbf{E}}_{GL}^e, \quad (10)$$

where $\tilde{\mathbf{C}}$ is the fourth-order anisotropic elasticity tensor, which can be expressed in terms of three parameters C_{11} , C_{12} and C_{44} for cubic elasticity.

In addition, the driving force for single crystal plasticity is known as the Mandel stress $\underline{\underline{M}}$, which is defined in the intermediate configuration and is work-conjugate to $\underline{\underline{L}}^p$:

$$\underline{\underline{M}} = J_e \underline{\underline{E}}^T \cdot \underline{\underline{\sigma}} \cdot \underline{\underline{E}}^{-T} = \underline{\underline{E}}^T \cdot \underline{\underline{E}} \cdot \underline{\underline{\Pi}}^e. \quad (11)$$

2.1.3. Flow rule

For each slip system, s , a yield function can be defined as:

$$\phi^s = \tau_s^* - \tau_c^s, \text{ with } \tau_s^* \geq 0 \quad (12)$$

where τ_s^* is a scalar stress and τ_c^s is the critical resolved shear stress (CRSS). For void-free single crystals, the scalar stress τ_s^* for system s is given by

$$\tau_s^* = \sqrt{\tau^s \tau^s} = |\tau^s|, \quad (13)$$

where τ^s is the resolved shear stress defined as:

$$\tau^s = \underline{\underline{M}} : \underline{\underline{N}}^s, \quad (14)$$

with the Schmid tensor $\underline{\underline{N}}^s = \underline{\underline{m}}^s \otimes \underline{\underline{n}}^s$ ($\underline{\underline{m}}^s$ is the slip direction vector and $\underline{\underline{n}}^s$ is the normal vector to the slip plane of slip system s). For each slip system, yielding occurs for $\phi^s \geq 0$.

The plastic strain rate $\underline{\underline{L}}^p$ can be defined as

$$\underline{\underline{L}}^p = \dot{\underline{\underline{P}}} \cdot \underline{\underline{P}}^{-1} = \sum_{s=1}^N \dot{\gamma}^s \frac{\partial \phi^s}{\partial \underline{\underline{M}}} = \sum_{s=1}^N \dot{\gamma}^s \underline{\underline{N}}^{*s}, \quad (15)$$

with $\underline{\underline{N}}^{*s}$

$$\underline{\underline{N}}^{*s} = \frac{\partial \phi^s}{\partial \underline{\underline{M}}} = \frac{\partial |\tau^s|}{\partial \tau^s} \frac{\partial \tau^s}{\partial \underline{\underline{M}}} = \text{sign}(\tau^s) \underline{\underline{N}}^s \quad (16)$$

and the plastic slip rate $\dot{\gamma}^s$ given by

$$\dot{\gamma}^s = \dot{\gamma}_0 \left(\frac{\tau_s^* - \tau_c^s}{\tau_0} \right)^n, \quad (17)$$

where $\dot{\gamma}_0$ is the reference slip rate and τ_0 the thermal component of the CRSS due to the lattice friction. Note that $\langle \bullet \rangle = \bullet$ if $\bullet > 0$, else $\langle \bullet \rangle = 0$.

2.1.4. Hardening rule

For the hardening rule, an evolution law involving dislocation densities as the only source of hardening is chosen. Following Kubin et al. (2008), the CRSS τ_c^s of the slip system s can be expressed as a function of dislocation densities ρ^s

$$\tau_c^s = \tau_0 + \mu b \sqrt{\sum_{u=1}^N a^{su} \rho^u}, \quad (18)$$

with τ_0 the thermal component of the CRSS due to the lattice friction, μ the shear modulus, b the norm of Burgers vector of dislocations and a^{su} the dislocation interaction matrix. Considering the multiplication and the annihilation of dislocations due to the interactions among them, the evolution of dislocation densities ρ^s is governed by

$$\dot{\rho}^s = \frac{1}{b} \left(\frac{1}{L^s} - g_c \rho^s \right) \dot{\gamma}^s, \quad (19)$$

with the proportionality factor g_c and the mean free path of dislocations L^s determined by

$$L^s = \kappa \left(\sum_{u=1}^N b^{su} \rho^u \right)^{-\frac{1}{2}}, \quad (20)$$

where κ is a proportionality factor and b^{su} is a second dislocation interaction matrix.

2.2. Porous single crystals

For porous single crystals, it is assumed that, in spite of the presence of pores inside the single crystal volume element and associated inhomogeneous deformation, a unique single crystal lattice orientation can be attributed to each material point. The definition of a unique isoclinic intermediate local configuration C_i is allowed by the existence of directors associated with lattice orientation. The uniqueness of the multiplicative decomposition of the deformation gradient $\tilde{\mathbf{F}} = \tilde{\mathbf{E}} \cdot \tilde{\mathbf{P}}$ thus remains. As a result, the kinematics of porous single crystals follows what is described in Section 2.1, except that $\det(\tilde{\mathbf{P}}) \neq 1$ as a result of compressibility of porous single crystals. The initial porous single crystal orientation is taken as that of the undeformed single crystal matrix.

The same number of slip systems N is attributed to each material point of the porous single crystal as the single crystal matrix. They have the same crystallographic definition as that of the undeformed single crystal matrix. For the flow rule, the yield criterion developed in the work of Han et al. (2013) for porous single crystals is used. The definition of effective resolved shear stress τ_s^* , derived by Han et al. (2013) in the infinitesimal strain framework, is extended to finite strain framework:

$$\Psi^s = \frac{\tau^{s2}}{\tau_s^{*2}} + \alpha \frac{2}{45} f_i \frac{M_{eq}^2}{\tau_s^{*2}} + 2q_1 f_i \cosh \left\{ q_2 \sqrt{\frac{3}{20}} \frac{M_m}{\tau_s^*} \right\} - 1 - q_2^2 f_i^2 \stackrel{def}{=} 0, \quad \tau_s^* \geq 0, \quad (21)$$

where M_m is the mean Mandel stress defined as $M_m = \frac{1}{3} \text{trace } \tilde{\mathbf{M}}$; M_{eq} is the equivalent Mandel stress defined as $M_{eq} = \sqrt{\frac{3}{2} \tilde{\mathbf{M}}' : \tilde{\mathbf{M}}'}$ with the deviatoric part of Mandel stress $\tilde{\mathbf{M}}' = \tilde{\mathbf{M}} - M_m \mathbf{1}$; f_i is the void volume fraction in the intermediate configuration and can be calculated as

$$f_i = 1 - \frac{1 - f_0}{\det \tilde{\mathbf{P}}}, \quad (22)$$

with the initial void volume fraction f_0 . Note that α , q_1 and q_2 are parameters to be identified. The yield function for each slip system, taking the same form of Eq. (13), follows

$$\phi^s = \tau_s^* - \tau_c^s \quad (23)$$

with the effective resolved shear stress τ_s^* defined above.

The plastic strain rate $\tilde{\mathbf{L}}^p$ is defined by

$$\tilde{\mathbf{L}}^p = \dot{\tilde{\mathbf{P}}} \cdot \tilde{\mathbf{P}}^{-1} = (1 - f_i) \sum_{s=1}^N \dot{\gamma}^s \frac{\partial \phi^s}{\partial \tilde{\mathbf{M}}} = (1 - f_i) \sum_{s=1}^N \dot{\gamma}^s \tilde{\mathbf{N}}^{*s}, \quad (24)$$

with $\tilde{\mathbf{M}}$ still defined by Eq. (11) and

$$\tilde{\mathbf{N}}^{*s} = \frac{\partial \tau_s^*}{\partial \tilde{\mathbf{M}}} = - \left(\frac{\partial \Psi^s}{\partial \tau_s^*} \right)^{-1} \frac{\partial \Psi^s}{\partial \tilde{\mathbf{M}}}, \quad (25)$$

where

$$\frac{\partial \Psi^s}{\partial \tau_s^*} = -2 \frac{\tau^{s2}}{\tau_s^{*3}} - \frac{4}{45} \alpha f_i \frac{M_{eq}^2}{\tau_s^{*3}} - 2 \sqrt{\frac{3}{20}} q_1 q_2 f_i \frac{M_m}{\tau_s^{*2}} \sinh \left(q_2 \sqrt{\frac{3}{20}} \frac{M_m}{\tau_s^*} \right) \quad (26)$$

and

$$\frac{\partial \Psi^s}{\partial \tilde{\mathbf{M}}} = 2 \frac{\tau^s}{\tau_s^{*2}} \tilde{\mathbf{N}}^s + \frac{2}{15} \alpha f_i \frac{1}{\tau_s^{*2}} \tilde{\mathbf{M}}' + \frac{2}{3} \sqrt{\frac{3}{20}} q_1 q_2 f_i \frac{\sinh \left(q_2 \sqrt{\frac{3}{20}} \frac{M_m}{\tau_s^*} \right)}{\tau_s^*} \tilde{\mathbf{1}}. \quad (27)$$

Note that $\tilde{\mathbf{L}}^p$ is corrected by the factor $1 - f_i$ resulting from the definition of τ_s^* in Eq. (21) which is obtained by the homogenisation in the matrix of porous single crystal excluding the pores. It corresponds to the vanishing plastic work in the pores (see Besson (2009, 2010)). When $f_i = 0$, the model of porous single crystals is reduced to that of void-free single crystals.

The hardening rule described in Section 2.1 holds for porous single crystals.

3. 3D FE unit cell simulations

Three-dimensional finite element unit cell simulations are carried out with the void-free single crystal model in order to assess the macroscopic porous single crystal model. The Zset FE software (Besson and Foerch (1998)) is used.

The unit cell Ω_0^{tot} considered is taken as a cubic matrix Ω_0^{mat} of side lengths $L = L_0$ with an initially spherical void $\Omega_0^{tot} \setminus \Omega_0^{mat}$ at the centre with radius $R_1 = R_2 = R_3 = R_0$ (see Fig. 1a). Thus, the initial void volume fraction f_0 is

$$f_0 = \frac{4}{3} \pi \frac{R_0^3}{L_0^3}. \tag{28}$$

The edges of the unit cell are initially parallel to the coordinate x_i -axes and the main loading direction is parallel to the x_1 axis. Different initial void volume fractions are taken into account for the simulations: $f_0 = 0.005, 0.01, 0.02, 0.05$ and 0.1 .

FCC single crystal lattice is considered with 12 slip systems. According to Schmid and Boas (1935), the slip systems of FCC single crystal are specified by the slip direction vector \underline{m}^s and the normal vector \underline{n}^s to the slip plane, which are summarised in Table 1. Each unit cell has a different crystal orientation characterised by the crystallographic orientations aligned with the three coordinate axes $x_1-x_2-x_3$. Five crystal orientations are considered: $[100]-[010]-[001]$, $[110]-[\bar{1}10]-[001]$, $[111]-[\bar{2}11]-[0\bar{1}1]$, $[210]-[\bar{1}20]-[001]$ and $[\bar{1}25]-[\bar{1}\bar{2}1]-[210]$. They have different symmetry about the coordinate planes and correspond to different number of primary slip systems activated in uniaxial tension (see Table 2). The crystal orientations are named in the following by the crystallographic orientation parallel to the main loading direction, i.e., $[100]$, $[110]$, $[111]$, $[210]$ and $[\bar{1}25]$.

The material parameters used for the following simulations are closely related to those of a solution annealed 304 austenitic stainless steel at 340°C (see Han (2012)). To be more precise, a^{su} is assumed to be identical for all $s, u = 1, \dots, 12$, b^{su} is

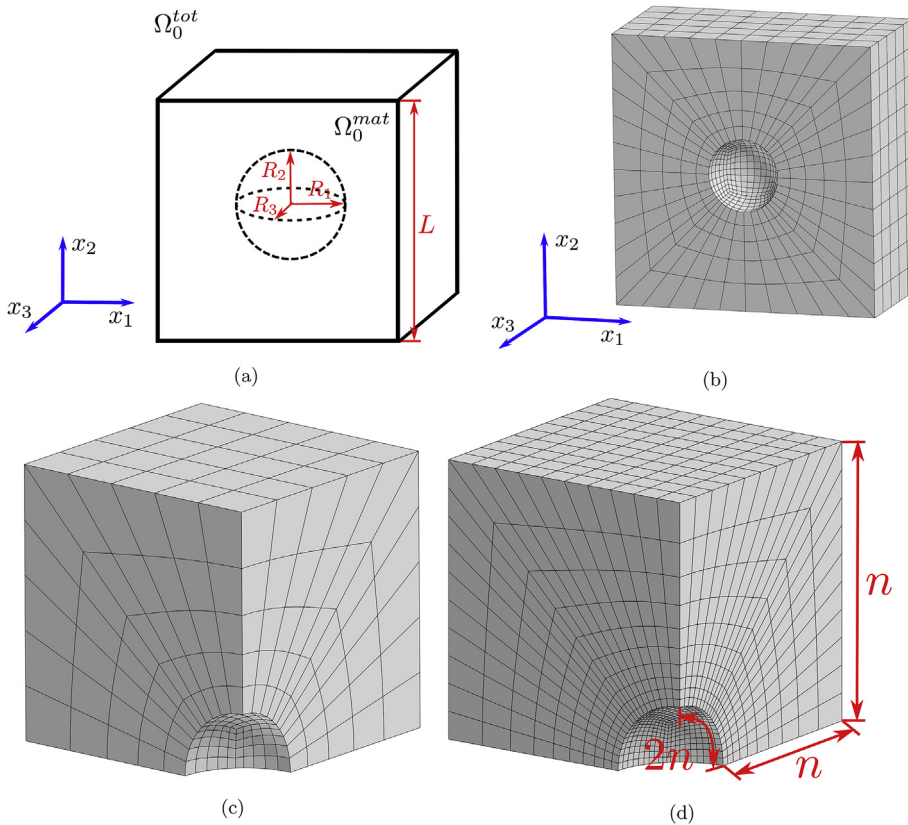


Fig. 1. Unit cell with an initially spherical void at the centre for initial void volume fraction $f_0 = 0.01$. (a) the geometry of the unit cell with $R_1 = R_2 = R_3 = R_0$ (b) a 3D mesh of half of the unit cell showing the initially spherical void (c) the coarse mesh ($n = 5$) for 1/8 of the full geometry (d) the fine mesh ($n = 10$) for 1/8 of the full geometry.

Table 1
Slip systems in FCC single crystals.

s	1	2	3	4	5	6	7	8	9	10	11	12
\underline{n}^s	(111)			($\bar{1}\bar{1}1$)			($\bar{1}11$)			($\bar{1}\bar{1}\bar{1}$)		
\underline{m}^s	$[\bar{1}01]$	$[0\bar{1}1]$	$[\bar{1}10]$	$[\bar{1}01]$	$[011]$	$[110]$	$[0\bar{1}1]$	$[110]$	$[101]$	$[\bar{1}10]$	$[101]$	$[011]$

Table 2
Crystal orientations and number of primary slip systems activated in uniaxial tension.

Orientation name	Crystallographic orientation along $x_1-x_2-x_3$	Number of primary slip systems
[100]	[100] – [010] – [001]	8
[110]	[110] – [110] – [001]	4
[111]	[111] – [211] – [011]	6
[210]	[210] – [120] – [001]	2
[125]	[125] – [121] – [210]	1

set equal to 0 if $s = u$ and equal to 1 if $s \neq u$, the initial value of dislocation density ρ_0^s is assumed to be identical for all slip systems and equal to $8.33 \times 10^8 \text{ m}^{-2}$. All the material parameters used for the simulations are given in Table 3.

3.1. FE formulation with prescribed triaxiality and periodic boundary conditions

Numerical periodic homogenisation is used for the simulations with periodic finite elements, which are enhanced by average strains as element degrees of freedom. In the following, variables at microscopic and macroscopic scale are distinguished. The variables with an overline symbol ($\bar{\cdot}$) are used for macroscopic scale at which an effective behaviour of the unit cell is observed, while the variables without the overline symbol describe the behaviour at microscopic scale, i.e., at each material point of the unit cell.

The unit cell is subjected to periodic boundary conditions, which is expressed by

$$\underline{\mathbf{u}} = \bar{\mathbf{F}} \cdot \underline{\mathbf{X}} + \underline{\mathbf{v}}, \quad (29)$$

where $\bar{\mathbf{F}}$ denotes the macroscopic deformation gradient field, $\underline{\mathbf{u}}$ the displacement vector and $\underline{\mathbf{v}}$ a periodic fluctuation vector, which follows

$$\underline{\mathbf{v}}(\underline{\mathbf{x}}^+) = \underline{\mathbf{v}}(\underline{\mathbf{x}}^-) \quad (30)$$

with the coordinates of homologous nodes ($\underline{\mathbf{x}}^+$, $\underline{\mathbf{x}}^-$) on opposite faces of the unit cell. The microscopic and macroscopic stress and deformation tensors are related by

$$\bar{\mathbf{S}} = \frac{1}{V_0^{\text{tot}}} \int_{\Omega_0^{\text{tot}}} \underline{\mathbf{S}} dV = (1 - f_0) \frac{1}{V_0^{\text{mat}}} \int_{\Omega_0^{\text{mat}}} \underline{\mathbf{S}} dV \quad (31)$$

and

$$\bar{\mathbf{F}} = \frac{1}{V_0^{\text{tot}}} \int_{\Omega_0^{\text{tot}}} \underline{\mathbf{F}} dV, \quad (32)$$

where V_0^{tot} and V_0^{mat} denote respectively the total volume of the unit cell and the volume of the matrix in the reference configuration, $\underline{\mathbf{S}}$ and $\bar{\mathbf{S}}$ denote respectively microscopic and macroscopic first Piola-Kirchhoff stress tensor.

The macroscopic Cauchy stress tensor $\bar{\boldsymbol{\sigma}}$ is related to the macroscopic first Piola-Kirchhoff stress tensor by

$$\bar{\boldsymbol{\sigma}} = \frac{1}{\bar{J}} \bar{\mathbf{S}} \cdot \bar{\mathbf{F}}^T, \quad (33)$$

with $\bar{J} = \det(\bar{\mathbf{F}})$.

Constant macroscopic Cauchy stress triaxiality T (the ratio of hydrostatic stress $\bar{\sigma}_m$ and equivalent stress $\bar{\sigma}_{eq}$ of macroscopic Cauchy stress $\bar{\boldsymbol{\sigma}}$) is imposed via a special truss element (see Section Appendix A), with

Table 3
Material parameters for the unit cell simulations (see Han (2012)).

C_{11}	C_{12}	C_{44}	τ_0	n	$\dot{\gamma}_0$	μ
199 GPa	136 GPa	105 GPa	88 MPa	15	$1.47 \times 10^{14} \text{ s}^{-1}$	65.6 GPa
g_c	κ	a^{su}	b^{su} ($s \neq u$)	b^{su} ($s = u$)	b	ρ_0^s
$2.6 \times 10^{-9} \text{ m}$	42.8	0.124	1	0	2.54 Å	$8.33 \times 10^8 \text{ m}^{-2}$

$$\bar{\sigma} = \begin{bmatrix} \bar{\sigma}_{11} & 0 & 0 \\ 0 & \bar{\sigma}_{22} & 0 \\ 0 & 0 & \bar{\sigma}_{33} \end{bmatrix} = \bar{\sigma}_{11} \begin{bmatrix} 1 & 0 & 0 \\ 0 & \eta_2 & 0 \\ 0 & 0 & \eta_3 \end{bmatrix} = \bar{\sigma}_{11} \bar{\sigma}_0, \quad (34)$$

such that

$$T = \frac{\bar{\sigma}_m}{\bar{\sigma}_{eq}} = \frac{1 + \eta_2 + \eta_3}{3\sqrt{1 - \eta_2 - \eta_3 - \eta_2\eta_3 + \eta_2^2 + \eta_3^2}}. \quad (35)$$

Axisymmetric loadings are mainly concerned, which implies that $\eta_2 = \eta_3 = \eta$, $0 \leq \eta \leq 1$ and that the imposed macroscopic Cauchy stress triaxiality is

$$T = \frac{1 + 2\eta}{3(1 - \eta)}. \quad (36)$$

Four levels of the stress triaxiality varying from 1 to 3 are chosen for axisymmetric loading. The details of the stress triaxiality T and corresponding values of η are summarised in Table 4. These relatively high stress triaxialities correspond to that involved in ductile failure zones, such as the vicinity of a crack tip.

Non-axisymmetric loading will not be presented in this part, but used for the assessment of the porous single crystal model in Section 5.3.

Prescribing periodic conditions for the considered unit cell means that a periodic distribution of voids is assumed, the voids occupying a simple cubic lattice in the present case. Periodic boundary conditions are applicable even if the crystal symmetry axes do not coincide with that of the geometric distribution of voids. However, it is not obvious that such a specific void distribution in the case of non-symmetric crystal orientations is realistic with respect to real physical situations of void growth in crystals. Random distributions of pores may provide different results. They should be studied in the future, as done for isotropic porous plasticity in Fritzen et al. (2012).

3.2. FE discretisation effect

The unit cell is meshed with reduced-integration quadratic hexahedral elements. A study of the effect of finite element discretisation was first conducted to optimise computation time while keeping sufficient accuracy. Due to the anisotropy of the matrix, complete unit cells are used for the simulations (see Fig. 1b for half of a complete mesh with the initial void volume fraction $f_0 = 0.01$). Two different finite element discretisations are considered as shown in Fig. 1c and d for one eighth of the FE mesh. The total number of elements used for the meshes can be calculated by $24 \times n^3$, where $n = 5$ (3000 elements) for the coarse mesh (Fig. 1c) and $n = 10$ (24,000 elements) for the fine mesh (Fig. 1d). The variable n is used to characterise the number of elements of the unit cell as shown in Fig. 1d. The crystallographic orientation [100] is chosen for this study with initial void volume fraction $f_0 = 0.01$ and two levels of stress triaxiality are considered: $T \in \{1, 3\}$.

The influence of the FE discretisation on the overall stress strain behaviour and the void volume fraction evolution is evaluated. The overall Cauchy stress $\bar{\sigma}$ is

$$\bar{\sigma} = \frac{1}{V^{tot}} \int_{\Omega^{tot}} \sigma dV = (1 - f) \frac{1}{V^{mat}} \int_{\Omega^{mat}} \sigma dV, \quad (37)$$

where V^{tot} and V^{mat} denote respectively the total volume of the unit cell Ω^{tot} and the volume of the matrix Ω^{mat} in the current configuration, and the void volume fraction f is calculated by

$$f = \frac{V^{tot} - V^{mat}}{V^{tot}}, \quad (38)$$

where the volume of the matrix V^{mat} in the actual configuration is calculated by a post-processing of Zset software and the total volume of the unit cell V^{tot} in the current configuration can be obtained as

$$V^{tot} = \det(\bar{\mathbf{F}}) V_0^{tot}, \quad (39)$$

with V_0^{tot} the initial volume of the unit cell.

Table 4
Values of the stress triaxiality T and η for axisymmetric loading.

η	0.4	0.538	0.625	0.727
T	1.0	1.5	2.0	3.0

The evolution of normalised macroscopic Cauchy stress component $\bar{\sigma}_{11}/\tau_0$ and the void volume fraction f with respect to the deformation in the main loading direction $\bar{F}_{11} - 1$ are shown in Fig. 2. It can be seen that the influence of FE discretisation on the overall stress strain behaviour and the evolution of void volume fraction is negligible for both low stress triaxiality ($T = 1$) and high stress triaxiality ($T = 3$). Even in the softening regime at $T = 3$, its influence is weak.

The coarse mesh ($n = 5$) is used for the simulations, except otherwise stated, to obtain the curves of the macroscopic Cauchy stress $\bar{\sigma}_{11}$ and the void volume fraction f .

4. Results of unit cell simulations

In this part, the results of the unit cell simulations with axisymmetric loading are presented. The most relevant results could be discussed after choosing the three following orientations: [100], [111] and $\bar{[125]}$ (see Table 2). [100] represents multiple slip orientation with mirror symmetry about three coordinate planes, [111] multiple slip orientation with mirror symmetry about the x_1-x_2 coordinate plane, and $\bar{[125]}$ represents single slip orientation with no mirror symmetry about the coordinate planes.

4.1. Overall stress strain response

Fig. 3a shows the overall stress strain response of the unit cell for the [100] orientation with $f_0 = 0.01$ and the stress triaxiality T varying from 1 to 3. The macroscopic stress $\bar{\sigma}_{11}$ is normalised with respect to τ_0 . It can be seen that the behaviour consists of a hardening regime followed by a softening regime, resulting from the competition between the strain hardening of matrix, the softening due to void growth and the softening due to void coalescence. The softening occurs earlier at high

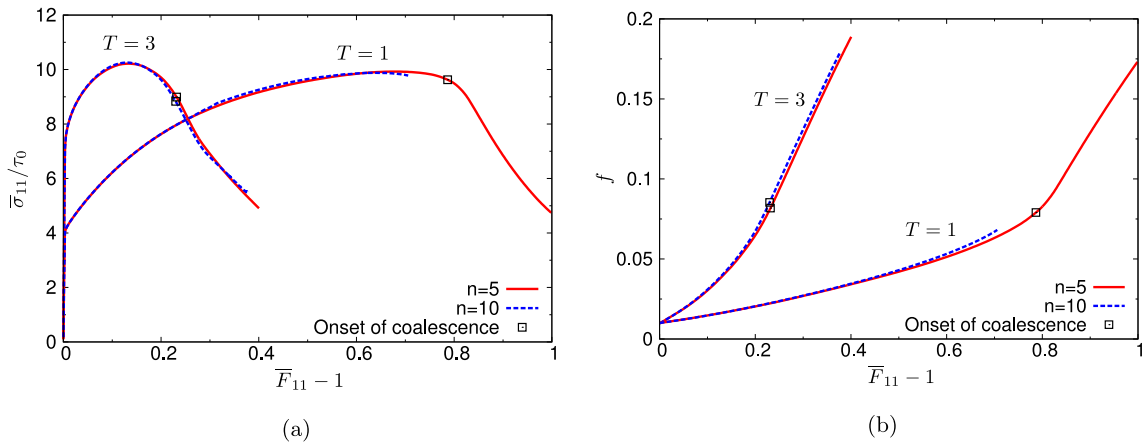


Fig. 2. FE discretisation effect on (a) the overall stress strain behaviour (b) the void volume fraction for the [100] orientation and $f_0 = 0.01$.

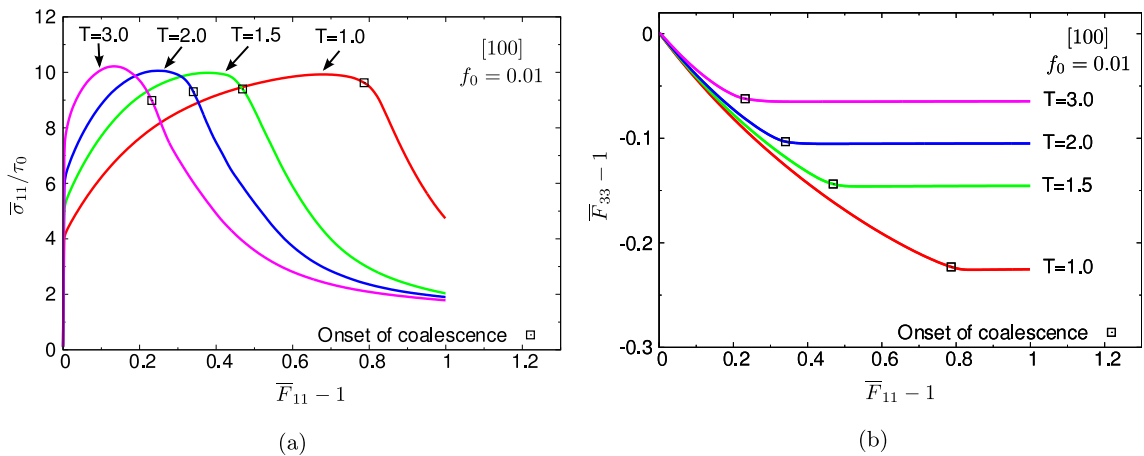


Fig. 3. Effect of stress triaxiality on the overall behaviour of the unit cell for the crystallographic orientation [100], $f_0 = 0.01$ and triaxiality T from 1 to 3: (a) overall stress–strain curves and (b) evolution of the transverse strain vs. longitudinal strain.

stress triaxiality compared to that at low stress triaxiality. This can be explained by faster void growth at higher stress triaxiality. According to [Koplik and Needleman \(1988\)](#), the onset of void coalescence is characterised by the transition to a uniaxial straining associated to the localisation of the plastic flow in the intervoid ligament. In this work, it is determined by comparing the transverse macroscopic strain $\bar{F}_{33} - 1$ with the longitudinal macroscopic strain $\bar{F}_{11} - 1$ through [Fig. 3b](#). A stabilized regime of the transverse strain $\bar{F}_{33} - 1$ can be observed in [Fig. 3b](#) and it corresponds to the regime of void coalescence. The time step, when the transverse strain $\bar{F}_{33} - 1$ reaches 99% of its stabilized value, is regarded as the onset of coalescence, and the corresponding longitudinal strain $\bar{F}_{11c} - 1$ is defined as the critical strain for the onset of coalescence. The onset of void coalescence is indicated by a hollow square on each curve. It can be observed that the critical strain $\bar{F}_{11c} - 1$ decreases when the stress triaxiality T increases. Void coalescence will be discussed in more details in [Section 4.6](#) in [Section 4.6](#).

The effect of crystallographic orientation on the overall behaviour is presented in [Fig. 4](#), where the five crystallographic orientations are considered with the initial void volume fraction $f_0 = 0.01$ and the stress triaxiality $T = 2$. The [111] orientation shows the hardest response and the orientations [210] and $\bar{1}\bar{1}2\bar{5}$ exhibit the softest response (see [Fig. 4a](#)). The peak stress depends on the orientation and this agrees with the results obtained by [Ha and Kim \(2010\)](#) for FCC single crystals and by [Yerra et al. \(2010\)](#) for BCC single crystals. In particular, the [110] orientation exhibits the highest peak stress and this is also observed by [Ha and Kim \(2010\)](#). As a general result, the softening regime starts earlier for the orientation [111] compared with the other orientations, which implies the fastest void growth for the [111] orientation, as confirmed in [Section 4.2](#). In addition, as shown in [Fig. 4b](#), the [111] orientation leads to the earliest onset of coalescence.

4.2. Void growth

[Fig. 5a](#) shows the effect of stress triaxiality on the evolution of void volume fraction f for the [100] orientation with the initial void volume fraction $f_0 = 0.01$ and the stress triaxiality T varying from 1 to 3. The results confirm the analysis of [Section 4.1](#): higher stress triaxiality leads to faster void growth, which induces earlier softening of the unit cell. These results are consistent with the observation of [Ha and Kim \(2010\)](#) for FCC single crystals.

The evolution of void volume fraction for different orientations with $f_0 = 0.01$ is presented in [Fig. 5b](#) for the stress triaxiality $T = 1$ and in [Fig. 5c](#) for the stress triaxiality $T = 3$. Generally, the void growth rate depends on the crystallographic orientation. The effect of crystallographic orientation is significant when the stress triaxiality is small ($T = 1$ as in [Fig. 5b](#)), which is in agreement with the results of [Yerra et al. \(2010\)](#) for BCC single crystals and those of [Ha and Kim \(2010\)](#) for FCC single crystals. However, the influence of the orientation becomes much weaker at high stress triaxiality ($T = 3$ as in [Fig. 5c](#)). Moreover, in both cases of $T = 1$ and $T = 3$, the void growth rate is significantly higher in the [111] orientation than the other orientations, which is in good agreement with the analysis in [Section 4.1](#). A significant result from this calculation is the very limited void growth and the quasi-incompressible response for the [210] and $\bar{1}\bar{1}2\bar{5}$ orientations at low stress triaxiality $T = 1$.

Void aspect ratios are also investigated, allowing to characterise the evolution of the void shape. The evolution of two aspect ratios $W_2 = R_1/R_2$ and $W_3 = R_3/R_1$ are presented in [Fig. 6a](#) for the [100] orientation and in [Fig. 6b](#) for the $\bar{1}\bar{1}2\bar{5}$ orientation with the initial void volume fraction $f_0 = 0.01$. R_i , $i = 1, 2, 3$ is the length from the centre of void to the node at the initial pole of the void surface in the x_i direction. Two levels of stress triaxiality $T = 1$ and $T = 3$ are considered here. For both orientations, the aspect ratios become larger than 1 before void coalescence at $T = 1$, which implies a void elongation in the main loading direction at low stress triaxiality. For the [100] orientation at $T = 3$, the void aspect ratios decrease without exceeding the value of 1 before the onset of coalescence, which is a consequence of the oblate shape of the void induced by

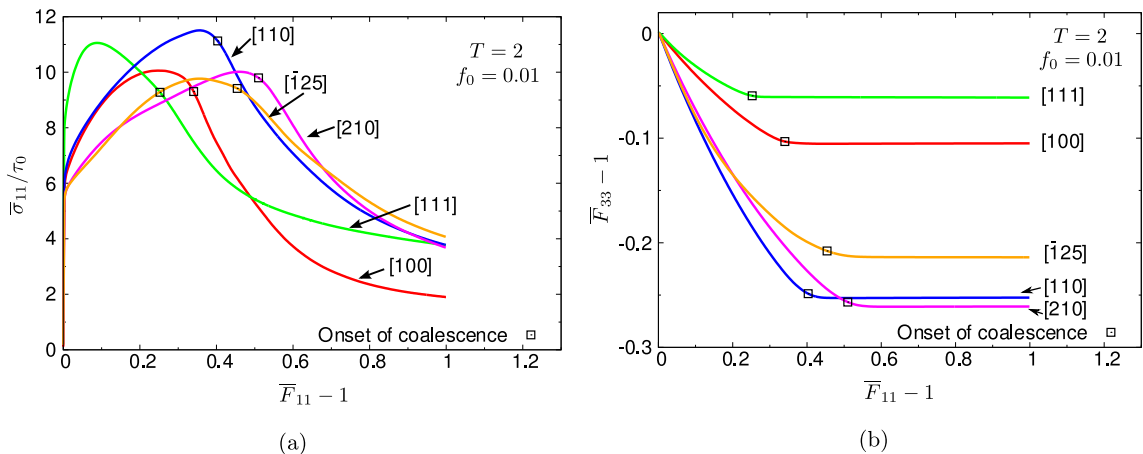


Fig. 4. Effect of crystallographic orientation on the overall behaviour of the unit cell for $f_0 = 0.01$, triaxiality $T = 2$ and different crystallographic orientations: (a) overall stress–strain curves and (b) evolution of the transverse strain vs. longitudinal strain.

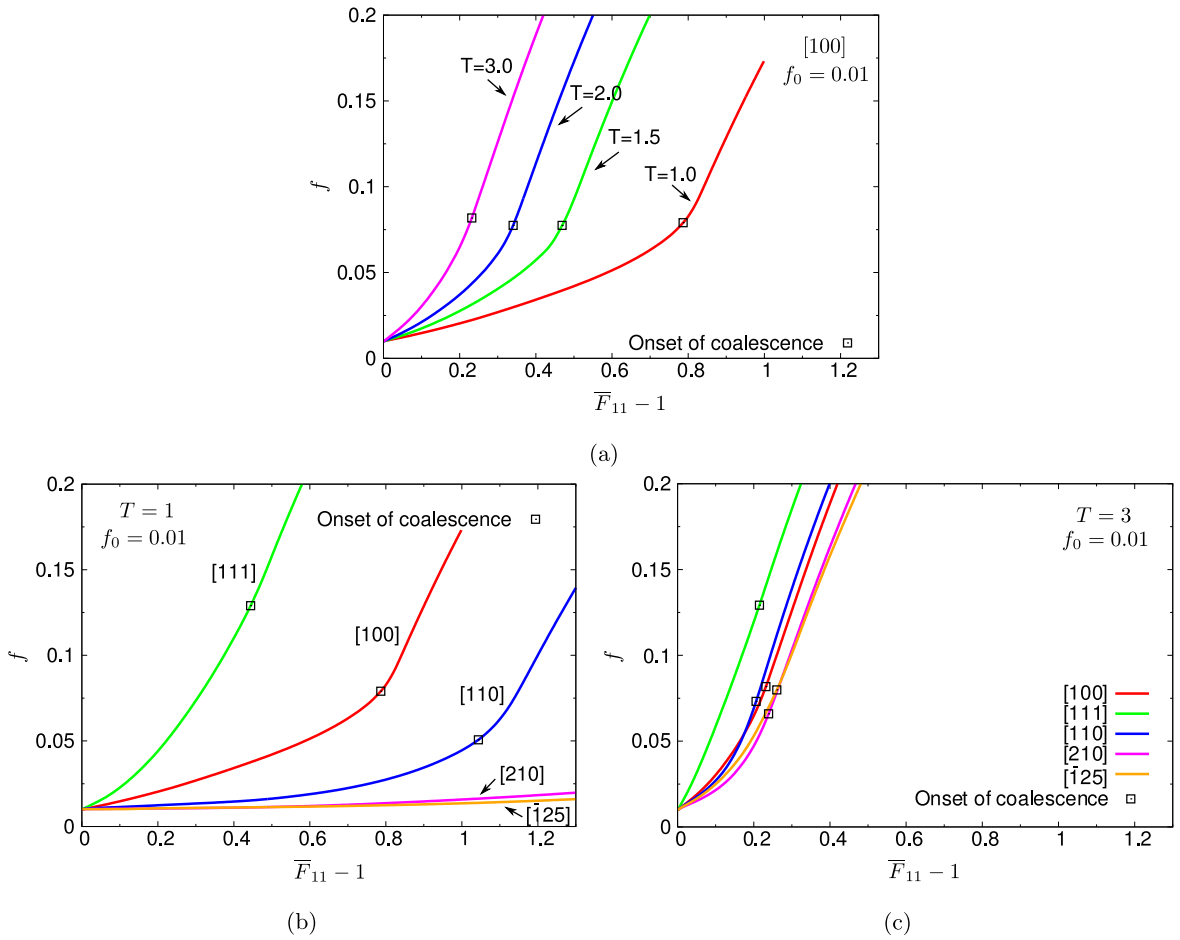


Fig. 5. Evolution of void volume fraction: (a) effect of stress triaxiality for crystallographic orientation [100], $f_0 = 0.01$ and triaxiality T from 1 to 3, (b) effect of crystallographic orientation for $f_0 = 0.01$ and stress triaxiality $T = 1$ and (c) effect of crystallographic orientation for $f_0 = 0.01$ and stress triaxiality $T = 3$.

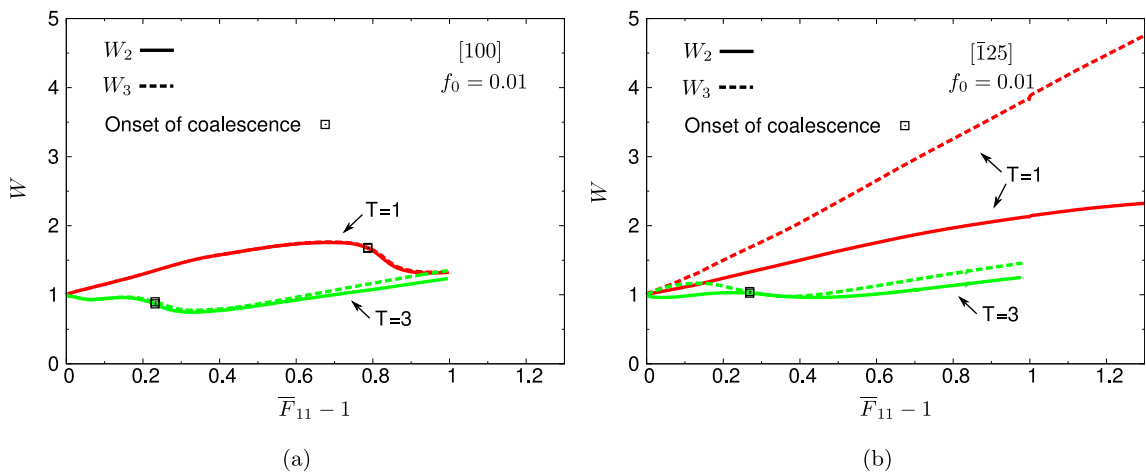


Fig. 6. Evolution of void aspect ratios W_2 and W_3 for (a) the crystallographic orientation [100] and (b) $\bar{1}25$ with triaxiality $T = 1$ and $T = 3$.

deformation. For the $\bar{1}25$ orientation at $T = 3$, the void aspect ratio W_2 remains close to 1 and W_3 becomes somewhat larger than 1 before the onset of coalescence. For symmetry reasons, W_2 is equal to W_3 for the [100] orientation at both high and low stress triaxiality. However, W_3 becomes much larger than W_2 for the $\bar{1}25$ especially at low stress triaxiality, which can be

explained by the anisotropy in the transverse plane x_2 – x_3 of the unit cell. It can also be observed that the difference in the evolution of the void aspect ratios between the [100] orientation and the $[\bar{1}25]$ orientation is much more significant at low stress triaxiality than that at high stress triaxiality.

4.3. Field of total cumulative slip

The total cumulative slip γ_{cum} , defined as

$$\gamma_{cum} = \sum_{s=1}^{12} \gamma^s, \quad (40)$$

is used to display the field of plastic slip around the void, and to explain some results obtained about void growth. The total cumulative slip fields in the middle x_1 – x_2 and x_1 – x_3 cross sections of the unit cell are shown for the stress triaxiality $T = 1$ in Fig. 7 and $T = 3$ in Fig. 8 with the [100], [111] and $[\bar{1}25]$ orientations and the initial void volume fraction $f_0 = 0.01$ at $\bar{F}_{11} - 1 = 0.1$. The fine mesh ($n = 10$, see Fig. 1d) is used to obtain the plastic slip field with more accurate local results. Recall that the macroscopic responses obtained with the fine mesh are identical to those with the coarse mesh, as shown in Section 3.2. For symmetry reasons, the surfaces of the unit cell remain planes and the unit cell keeps its cubic shape during loading for the [100] orientation. For the other orientations, the unit cell does not remain cubic during loading, as a result of lattice re-orientation and shearing of the mesh.

It can be observed that for each configuration (crystallographic orientation and stress triaxiality) a different pattern of plastic slip localisation will develop. For example, for the [100] orientation at $T = 1$ and $T = 3$, the unit cell shows a symmetric cross shaped localisation zone and the field in the x_1 – x_2 cross section is the same as that in the x_1 – x_3 cross section, as expected from matrix material symmetries. However, such symmetry is not observed for the two other orientations. For almost all six cases, the plastic slip is highly localised around the void, i.e., the red zone, except for the $[\bar{1}25]$ orientation at $T = 1$, where the localisation around the void is much weaker. A zone where no slip system is activated, i.e., the blue zone, is observed in all cases, except for the $[\bar{1}25]$ orientation at $T = 1$. In the case of the $[\bar{1}25]$ orientation at $T = 1$, the activation of the slip systems is nearly homogeneous in the matrix and it is found that only one slip system is activated almost everywhere in the matrix except in the vicinity of the void. One can conclude that the plastic slip heterogeneity introduced by the void in the matrix is negligible for the $[\bar{1}25]$ orientation at low stress triaxiality, but that the plastic slip heterogeneity will increase with stress triaxiality.

Figs. 7 and 8 also show the void shape at $\bar{F}_{11} - 1 = 0.1$. The elongation of the void in the x_1 axes can be observed at $T = 1$ for the three orientations. For the [100] orientation at $T = 3$, the void evolves into a polygon-like shape. For [111] at $T = 3$, the void is of lemon-like shape in the x_1 – x_2 cross section and polygon-like in the x_1 – x_3 cross section. For $[\bar{1}25]$ at $T = 3$, one can see that the cut of the void in the x_1 – x_2 cross section is almost a circle, i.e. $R_1 = R_2$ remains, however the void is elongated in the x_1 – x_3 cross section. These results are in good agreement with the results shown in Fig. 6.

4.4. Field of lattice rotation

The polar decomposition of the elastic part of deformation gradient $\underline{\underline{E}}$ follows

$$\underline{\underline{E}} = \underline{\underline{R}} \cdot \underline{\underline{U}}, \quad (41)$$

with the rotation tensor $\underline{\underline{R}}$ and the right stretch tensor $\underline{\underline{U}}$. Neglecting the elastic distortion $\underline{\underline{U}}$, $\underline{\underline{R}}$ can be interpreted as the lattice rotation. The corresponding rotation angle θ is given by

$$\theta = \arccos \frac{1}{2} \left(\text{trace } \underline{\underline{R}} - 1 \right). \quad (42)$$

The fields of θ (in radian) in the middle x_1 – x_2 and x_1 – x_3 cross sections are shown for the [100], [111] and $[\bar{1}25]$ orientations with the initial void volume fraction $f_0 = 0.01$ and the stress triaxiality $T = 1$ in Fig. 10 and $T = 3$ in Fig. 11 at $\bar{F}_{11} - 1 = 0.1$. At $T = 1$, lattice rotation occurs mainly around the void for [100] and [111], while it is almost homogeneous in the matrix for $[\bar{1}25]$. This is consistent with the fields of total cumulative slip observed in Section 4.3. For $[\bar{1}25]$, the quasi-homogeneous lattice rotation in the matrix leads to void-free-like macroscopic behaviour of the unit cell, i.e., the unit cell exhibits nearly pure shear, for a single slip orientation, in terms of macroscopic deformation pattern. At $T = 3$, the lattice rotation around the void is more significant compared with that at $T = 1$. In particular, the field of θ is no longer quasi-homogeneous for the $[\bar{1}25]$ orientation and the macroscopic deformation deviates from homogeneous shear.

4.5. Slip sectors

The number of activated slip systems around the hole during void growth is investigated. In the simulations, plastic deformation generally begins in single slip in some specific locations near the void. The plastic regions then expand and single

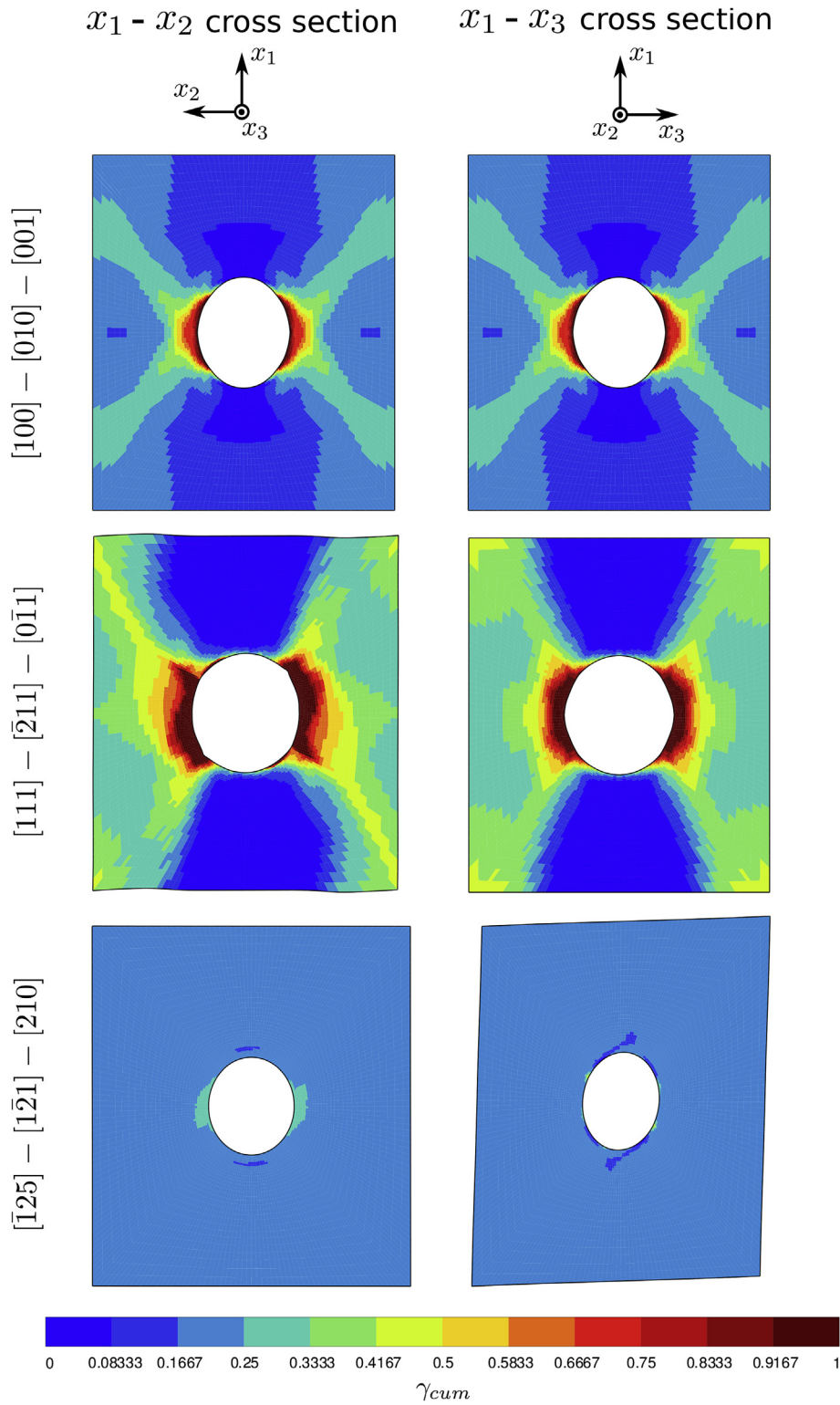


Fig. 7. Fields of accumulated plastic slip γ_{cum} in the x_1-x_2 (left column) and x_1-x_3 (right column) cross sections of the fine unit cell mesh ($n=10$) for three crystallographic orientations and stress triaxiality $T=1$ with the overall deformation $\bar{F}_{11}-1=0.1$. The initial void fraction is $f_0=0.01$.

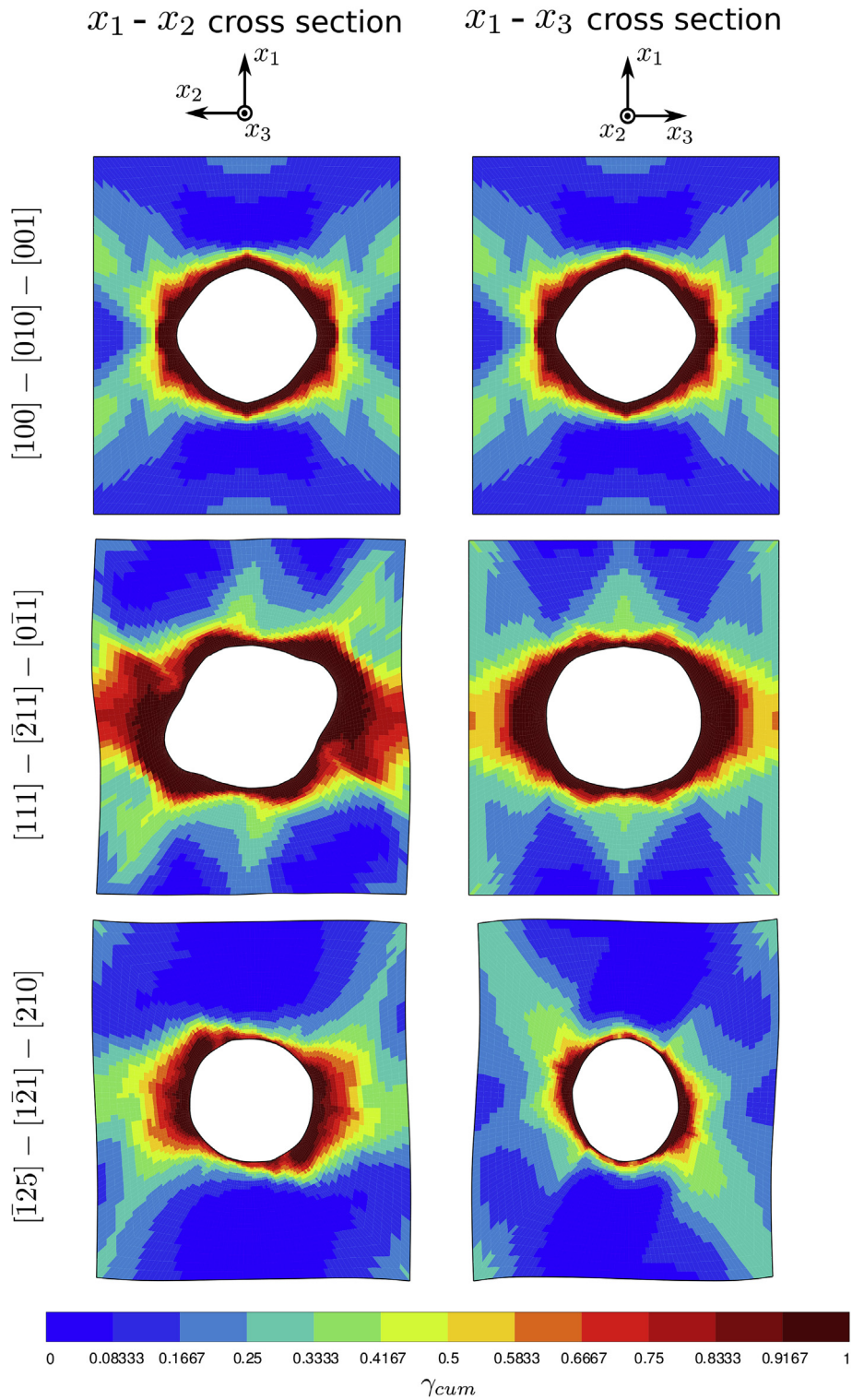


Fig. 8. Fields of accumulated plastic slip γ_{cum} in the $x_1 - x_2$ (left column) and $x_1 - x_3$ (right column) cross sections of the fine unit cell mesh ($n = 10$) for three crystallographic orientations and stress triaxiality $T = 3$ with the overall deformation $F_{11} - 1 = 0.1$. The initial void fraction is $f_0 = 0.01$.

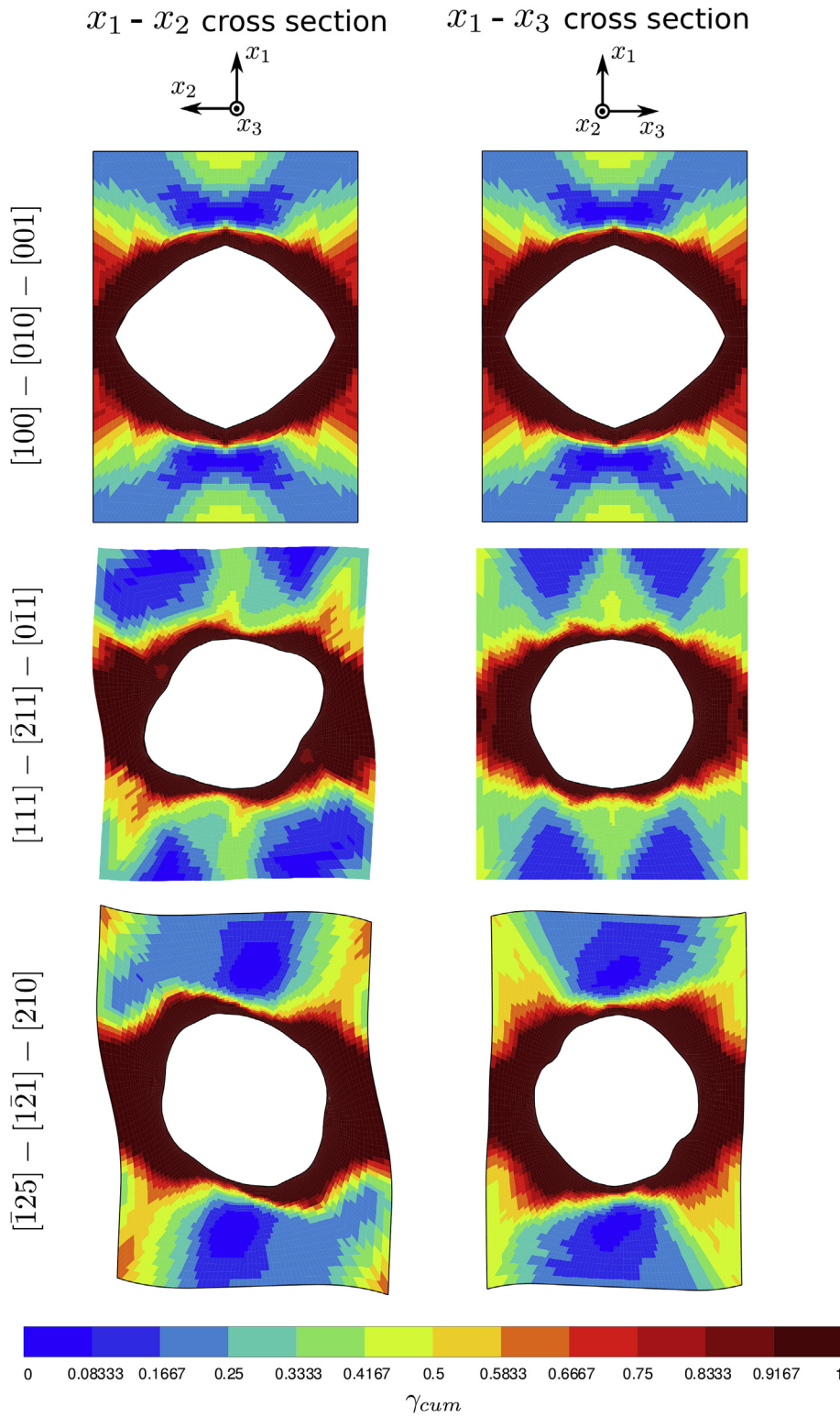


Fig. 9. Fields of accumulated plastic slip γ_{cum} in the $x_1 - x_2$ (left column) and $x_1 - x_3$ (right column) cross sections of the fine unit cell mesh ($n = 10$) for three crystallographic orientations and stress triaxiality $T = 3$. The overall deformation $\bar{F}_{11} - 1 = 0.29$ for $[100]$, $\bar{F}_{11} - 1 = 0.16$ for $[111]$ and $\bar{F}_{11} - 1 = 0.29$ for $[\bar{1}25]$. The current void fraction is $f \approx 0.1$ and the initial void fraction $f = 0.01$.

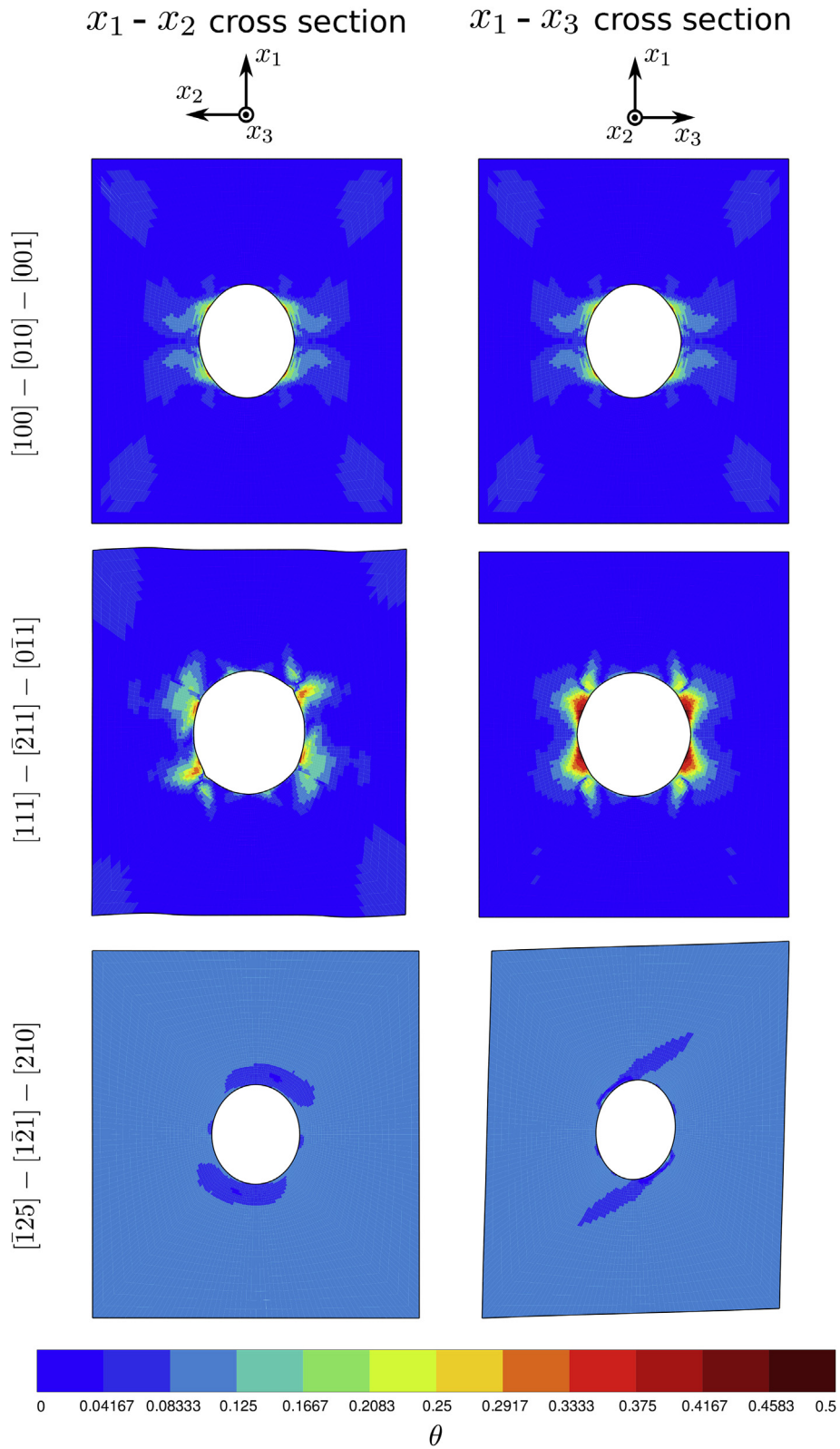


Fig. 10. Lattice rotation θ (in radian) in the x_1-x_2 (left column) and x_1-x_3 (right column) cross sections of the fine unit cell mesh ($n = 10$) for three crystallographic orientations and stress triaxiality $T = 1$ with the overall deformation $\bar{F}_{11} - 1 = 0.1$. The initial void fraction is $f_0 = 0.01$.

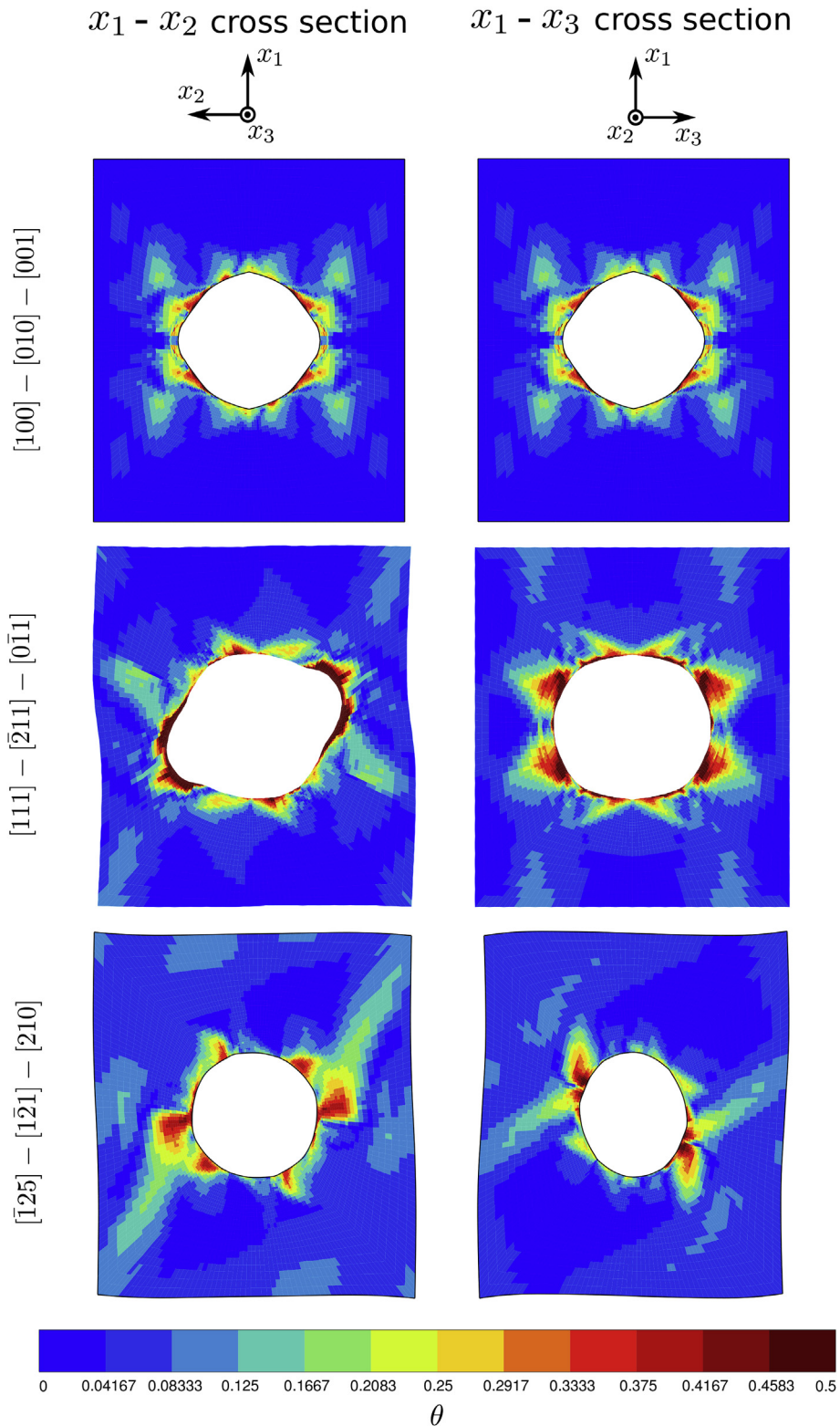


Fig. 11. Lattice rotation θ (in radian) in the x_1-x_2 (left column) and x_1-x_3 (right column) cross sections of the fine unit cell mesh ($n = 10$) for three crystallographic orientations and stress triaxiality $T = 3$ with the overall deformation $\bar{F}_{11} - 1 = 0.1$. The initial void fraction is $f_0 = 0.01$.

slip quickly evolves into multiple slip. The transition of slip sectors from single slip to multiple slip is closely related to strain hardening in the matrix. These results can be compared to the computations by Kysar et al. (2005) performed in the case of a cylindrical hole and mostly in the absence of hardening. For that purpose, the number of activated slip systems is shown in Fig. 12 in the first layer of elements bounding the void at $\bar{F}_{11} - 1 = 0.005$ for $T = 1$ and at $\bar{F}_{11} - 1 = 0.003$ for $T = 3$, before a strong change in the void shape occurs. The $[100]$, $[111]$ and $[\bar{1}25]$ orientations are considered. Sectors of slip activity display

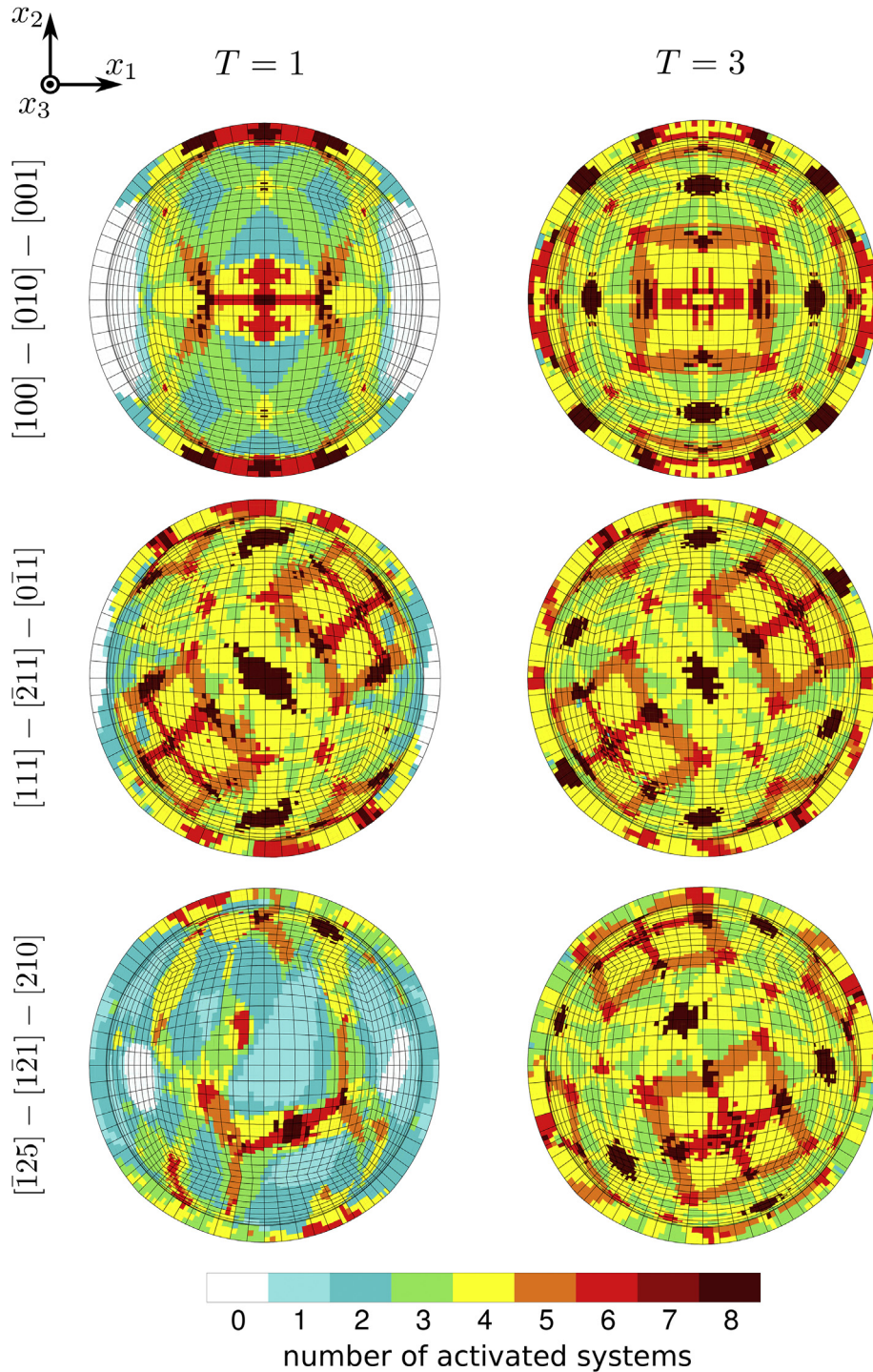


Fig. 12. Slip sectors for the different orientations in the elements bounding the void for $T = 1$ at $\bar{F}_{11} - 1 = 0.005$ and for $T = 3$ at $\bar{F}_{11} - 1 = 0.003$. Half of the void is shown.

regular geometrical structures determined by the crystallographic orientation and the stress triaxiality. For the three orientations with the stress triaxiality $T = 1$, plastic slip occurs in some parts near the void but the rest remains elastic. The structures of slip sectors, including their geometry and the number of activated systems, vary from one orientation to another. For higher stress triaxiality $T = 3$, the slip sectors cover the whole void for the three orientations. It can be seen that the slip sectors of the different orientations then display very similar structure (both the geometry and the number of activated systems) with only an orientation deviation between them.

For the different orientations, the multiple slip sectors are shown to be different at $T = 1$ but similar at $T = 3$. This observation is consistent with that on the total cumulative slip given in the Section 4.3, which shows the different slip localisation modes at $T = 1$ but the plastic slip taking place all around the void for all the orientations considered at $T = 3$. These results can be related to the significant orientation effects on void growth at $T = 1$ and the limited effects at $T = 3$.

4.6. Void coalescence

As explained in Section 4.1, the onset of void coalescence is determined by comparing the transverse strain with the longitudinal strain. However, for the asymmetric orientations, especially $[210]$ and $[\bar{1}25]$, the straining of the unit cell along the loading axis is accompanied by shearing, and the transverse straining of the unit cell may stop only along one transverse axis (x_2 or x_3 axis), which is interpreted as the preferred direction of coalescence. In that case, the onset of coalescence is determined by the preferred coalescence direction.

Fig. 13a presents the evolution of the critical strain $\bar{F}_{11c} - 1$ for the onset of void coalescence with respect to the stress triaxiality T for different orientations with the initial void volume fraction $f_0 = 0.01$. For the $[210]$ and $[\bar{1}25]$ orientations, the simulations are not able to provide coalescence at low stress triaxiality, even though the longitudinal macroscopic strain $\bar{F}_{11c} - 1$ reaches 130%. This is related to extremely low void growth rate for these two orientations at low stress triaxiality. For all the orientations, the critical strain $\bar{F}_{11c} - 1$ decreases with increasing stress triaxiality T . This result agrees with the observation of Yerra et al. (2010) for BCC single crystals. The difference of the critical strain $\bar{F}_{11c} - 1$ between different orientations is significant at low stress triaxiality, but less noticed at high stress triaxiality.

Once the critical strain $\bar{F}_{11c} - 1$ for the onset of void coalescence has been determined, the corresponding critical void volume fraction f_c for the void coalescence can readily be obtained. In Fig. 13b, the critical void volume fraction f_c is plotted as a function of stress triaxiality T for different orientations with $f_0 = 0.01$. With the stress triaxiality T varying from 1 to 3, the critical void volume fraction f_c appears sensitive to the orientation but almost not sensitive to triaxiality. As f_c is nearly constant and void growth is more rapid at high stress triaxiality, the onset of coalescence occurs at smaller values of macroscopic deformation for high stress triaxiality. These results motivate the introduction of a criterion for the onset of void coalescence in single crystals which can incorporate the strong dependence of the critical void volume fraction on the crystallographic orientation. This feature is not accounted for by any of the existing models for porous single crystals.

A remarkable feature of the coalescence modes observed in the case of non-symmetric crystal orientations is that the usual extension mode is accompanied by a strong overall shear component. These anisotropic coalescence modes are visible on Fig. 8 at the onset of coalescence and on Fig. 9 at a later deformation stage, especially for the $[111]$ orientation.

The above results are presented only for one initial void volume fraction $f_0 = 0.01$. Unit cell simulations with larger or smaller initial void volume fractions show similar influences of stress triaxiality and crystallographic orientation on the

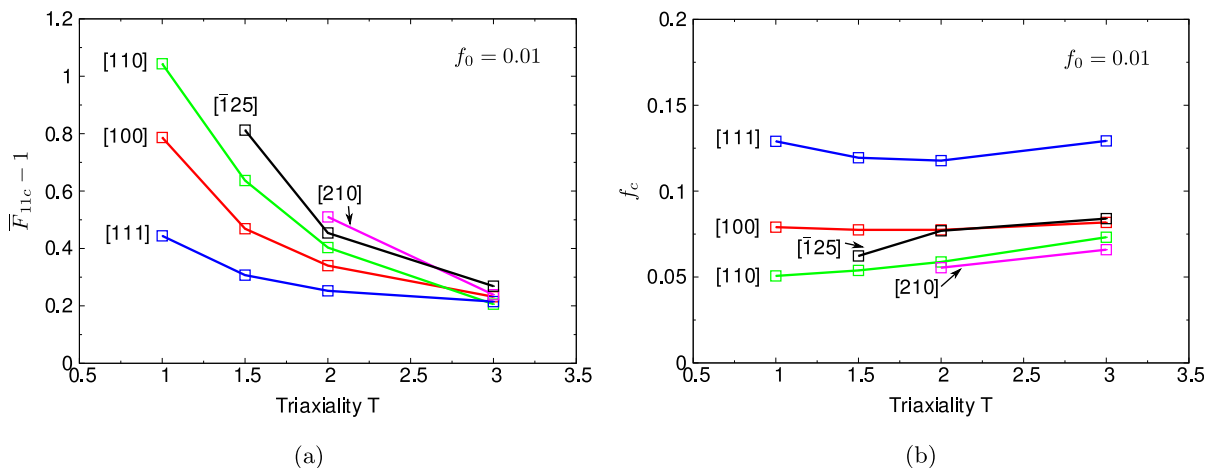


Fig. 13. Effect of stress triaxiality and crystallographic orientation on (a) the critical deformation $\bar{F}_{11c} - 1$ and (b) the critical void volume fraction f_c at the onset of coalescence for various crystallographic orientations and fixed initial void volume fraction $f_0 = 0.01$.

overall stress strain response and void evolution. For the sake of clarity, these results have not been reported in this section, but they will be used for the assessment of the macroscopic porous single crystal model presented in the next section.

5. Assessment of the porous single crystal model to void growth

5.1. Calibration of model parameters

The overall stress strain curves and the evolution of the void volume fraction obtained by the unit cell simulations with axisymmetric loading are used for calibrating the parameters α , q_1 and q_2 in Eq. (21) of the macroscopic porous single crystal model. The calibration has been conducted for a solution annealed 304 austenitic stainless steels with the material parameters given in Table 3. The crystallographic orientations, the initial void volume fractions f_0 and the stress triaxialities T considered for the calibration are summarised in Table 5.

The parameters α , q_1 and q_2 have been identified using Levenberg–Marquardt algorithm and taking into account at the same time the stress–strain response and the evolution of void volume fraction by minimizing the cost function:

$$\mathcal{F} = \frac{1}{F_{11}^t} \int_0^{F_{11}^t} w_1(\sigma_{11} - \bar{\sigma}_{11})^2 + w_2(f_i - f)^2 dF_{11}, \tag{43}$$

where σ_{11} denotes the component of Cauchy stress tensor of the porous single crystal model, $\bar{\sigma}_{11}$ the component of the macroscopic Cauchy stress tensor of the unit cell, f_i the void volume fraction of the porous single crystal model defined by Eq. (22) and f the void volume fraction predicted by the unit cell simulations (see Eq. (38)). F_{11}^t is chosen to be 1.1, i.e., the calibration is done from the beginning of the loading to the strain value $F_{11} - 1 = 0.1$ (for the porous single crystal model) and $\bar{F}_{11} - 1 = 0.1$ (for the unit cell). This level of macroscopic deformation corresponds to the regime before void coalescence for all the cases considered. In addition, the weight w_1 and w_2 are chosen in such a way that stress and void volume fraction have the same order of contribution to the cost function.

Optimised values of the parameters are given in Table 6. Note that the obtained calibrated parameters, accounting for the hardening of the matrix and the evolution of the void volume fraction, are slightly different from those determined by Han et al. (2013), where only the yield surface was taken into account. Comparison between the porous single crystal with the calibrated values of the parameters and the unit cell will be presented in the next sections.

5.2. Assessment for axisymmetric loading cases

In this part, the porous single crystal model is assessed for axisymmetric loading cases, which were used to calibrate the model parameters.

5.2.1. Comparison for stress strain responses

Fig. 14 shows the evolution of the normalised Cauchy stress σ_{11}/τ_0 with respect to the strain $F_{11} - 1$ for the porous single crystal model and that of the normalised macroscopic Cauchy stress $\bar{\sigma}_{11}/\tau_0$ with respect to the macroscopic strain $\bar{F}_{11} - 1$ for the unit cell for [100], [111] and $\bar{1}25$ orientations with $f_0 = 0.01$ at (a) $T = 1$ and (b) $T = 3$. To simplify the notation, the overline for the macroscopic variables of the unit cell will be dropped in the following (e.g., F_{11} instead of \bar{F}_{11}). As void coalescence is not incorporated in the porous single crystal model, the curves are plotted before void coalescence predicted by the unit cell simulations. At low stress triaxiality $T = 1$, the porous single crystal model successfully predicts the tendency of the

Table 5

Crystallographic orientations, initial void volume fractions and stress triaxialities used for the calibration of material parameters α , q_1 and q_2 , see Eq. (21).

Test number	Crystallographic orientation	Initial void volume fractions	Stress triaxialities
1	[100]–[010]–[001]	0.005, 0.01, 0.02, 0.05, 0.1	1.0, 1.5, 2.0, 3.0
2	[110]– $\bar{1}10$ –[001]	0.005, 0.01, 0.02	1.0, 1.5, 2.0, 3.0
3	[111]– $\bar{2}11$ – $\bar{0}11$	0.005, 0.01, 0.02, 0.05, 0.1	1.0, 1.5, 2.0, 3.0
4	$\bar{2}10$ – $\bar{1}20$ –[001]	0.005, 0.01, 0.02	1.0, 1.5, 2.0, 3.0
5	$\bar{1}25$ – $\bar{1}\bar{2}1$ – $\bar{2}10$	0.005, 0.01, 0.02, 0.05, 0.1	1.0, 1.5, 2.0, 3.0

Table 6

Identified values of the porous single crystal model parameters, see Eq. (21).

α	q_1	q_2
5.69	1.60	1.19

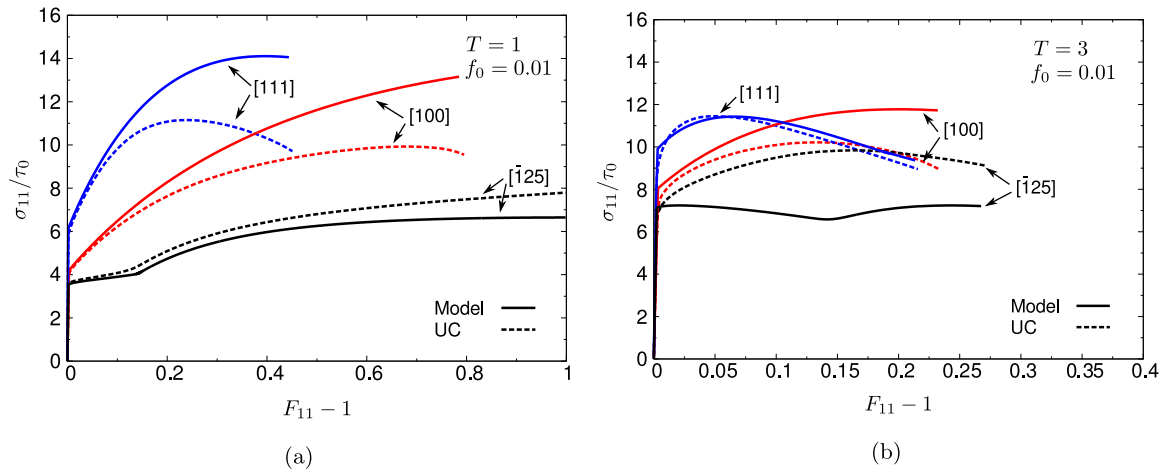


Fig. 14. Comparison between the unit cell (UC) simulations and the porous single crystal model predictions: evolution of normalised macroscopic stress σ_{11}/τ_0 with respect to axial strain $F_{11}-1$ for different crystallographic orientations with fixed triaxiality, (a) $T = 1$ and (b) $T = 3$, and initial void volume fraction $f_0 = 0.01$.

orientation effect on the stress strain response. However the model slightly overestimates the strain hardening for the [100] and [111] orientations and underestimates the strain hardening for the $\bar{1}25$ orientation. This can imply that the model will underestimate the void growth for the [100] and [111] orientations and overestimate the void growth for the $\bar{1}25$ orientation, which will be confirmed in the next section. At high stress triaxiality $T = 3$, the prediction of the model for the [111] orientation is generally in good agreement with the unit cell simulations, while the difference between the model and the unit cell simulation for the $\bar{1}25$ orientation is more significant.

The comparison of the stress strain response is also shown in Fig. 15 for larger initial void volume fraction $f_0 = 0.05$. Similar trends can be observed, except for an increased difference between the unit cell and the model for the $\bar{1}25$ orientation at low triaxiality $T = 1$ for this higher initial void volume fraction.

5.2.2. Comparison for void growth

Fig. 16 shows the comparison of the evolution of the void volume fraction f for three orientations with $f_0 = 0.01$ at stress triaxiality (a) $T = 1$ and (b) $T = 3$. It can be observed that the porous single crystal model satisfactorily describes the tendency of the orientation effect on the evolution of the void volume fraction at both low and high stress triaxiality. However, the model underestimates the void growth for the [100] and [111] orientations, and overestimates the void growth for the $\bar{1}25$ orientation at low stress triaxiality $T = 1$. These discrepancies are consistent with those presented in the previous section. At high stress triaxiality $T = 3$, the model well predicts the void growth for the [100] and $\bar{1}25$ orientations, but overestimates the void growth for the [111] orientation, which is probably related to the strong void distortion observed in Figs. 7–9.

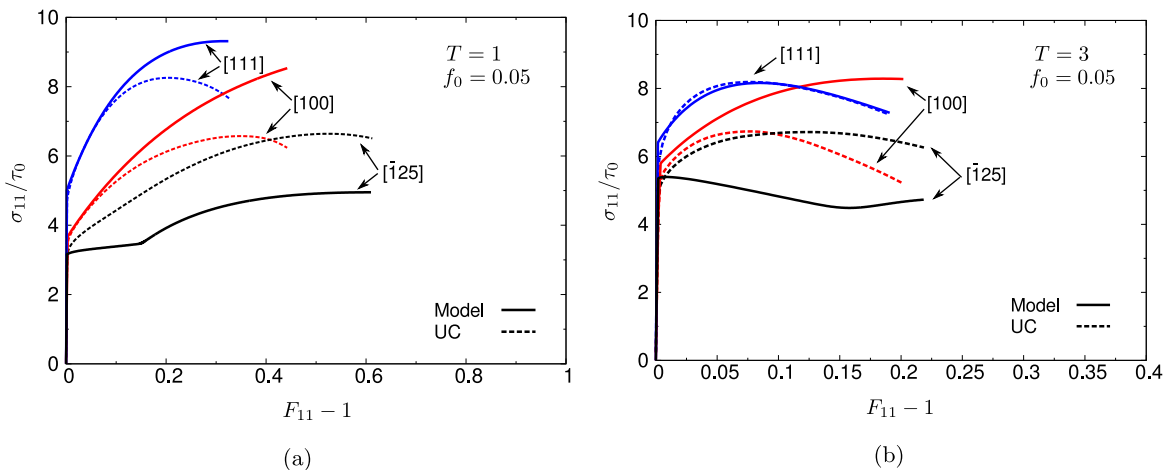


Fig. 15. Comparison between the unit cell simulations and the porous single crystal model predictions: evolution of normalised macroscopic stress σ_{11}/τ_0 with respect to axial strain $F_{11}-1$ for various crystallographic orientations with fixed triaxiality, (a) $T = 1$ and (b) $T = 3$, and initial void volume fraction $f_0 = 0.05$.

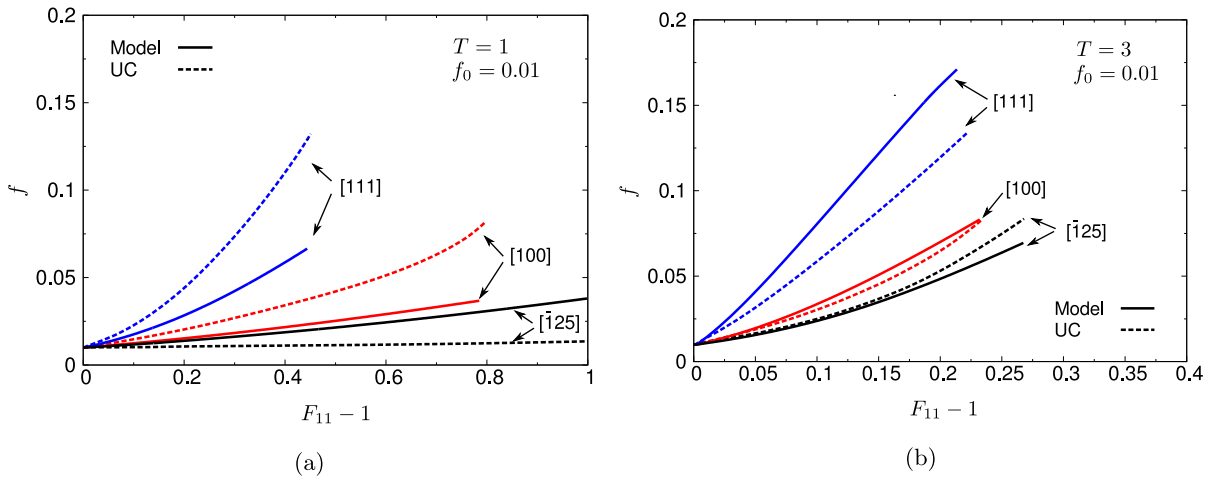


Fig. 16. Comparison between the unit cell simulations and the porous single crystal model predictions: evolution of void volume fraction f with respect to axial strain $F_{11}-1$ for various crystallographic orientations with fixed triaxiality, (a) $T = 1$ and (b) $T = 3$, and initial void volume fraction $f_0 = 0.01$.

The same comparison for larger initial void volume fraction $f_0 = 0.05$ is shown in Fig. 17. Similar results are found, i.e., the model well predicts the orientation effect on the evolution of void volume fraction. However, the model underestimates the void growth in the case of the $\bar{[125]}$ orientation at low stress triaxiality $T = 1$.

5.3. Assessment for non-axisymmetric loading cases

The porous single crystal model calibrated from the axisymmetric loading cases is used to predict macroscopic stress-strain behaviour and void volume fraction evolution under non-axisymmetric loadings in this part. The loadings with $\eta_2 = 0.727$ and $\eta_3 \in \{0.4, 0.538, 0.625\}$ are considered for the [100], [111] and $\bar{[125]}$ orientations with $f_0 = 0.01$.

The stress-strain responses predicted by the porous single crystal are compared to those of unit cell simulations in Fig. 18. In spite of insufficient strain hardening for the [111] and the $\bar{[125]}$ orientations, the model satisfactorily describes, for the non-axisymmetric loadings considered, the hierarchy of stress-strain response with respect to crystallographic orientation. For example, the [111] orientation shows the hardest response while the $\bar{[125]}$ orientation has the softest response.

The assessment of the porous single crystal model in terms of void volume fraction evolution is presented in Fig. 19. The hierarchy of void volume fraction evolution with respect to crystallographic orientation is well predicted by the model. In addition, for the [111] orientation with $\eta_2 = 0.727$ and $\eta_3 = 0.4$, the unit cell simulation displays low void growth. This situation is poorly captured by the model that predicts significant void growth and in turn insufficient hardening. This discrepancy has not been observed for the axisymmetric loading cases with this orientation at $\eta_2 = \eta_3 = 0.4$ ($T = 1$) in Figs. 14a

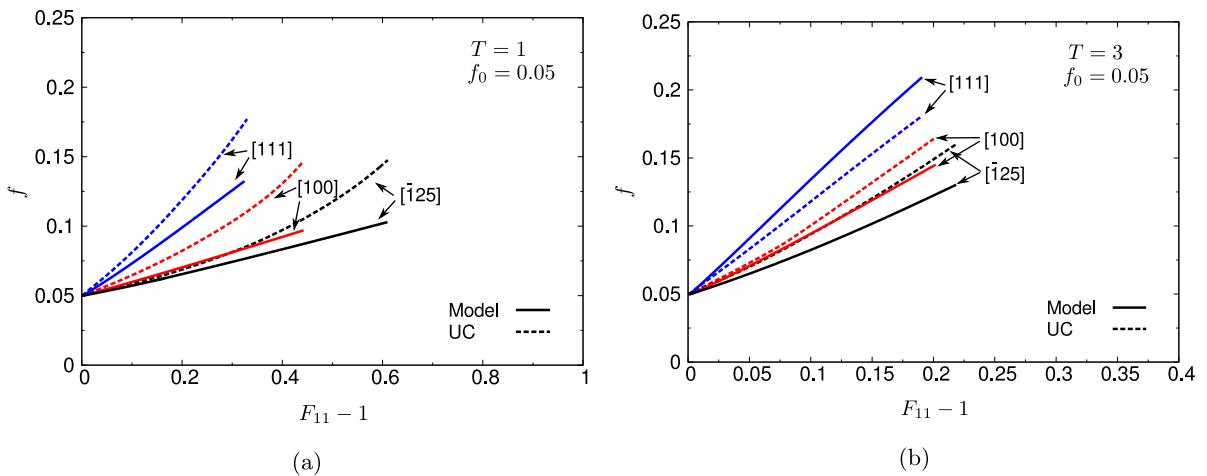


Fig. 17. Comparison between the unit cell simulations and the porous single crystal model predictions: evolution of void volume fraction f with respect to axial strain $F_{11}-1$ for various crystallographic orientations with fixed triaxiality, (a) $T = 1$ and (b) $T = 3$, and initial void volume fraction $f_0 = 0.05$.

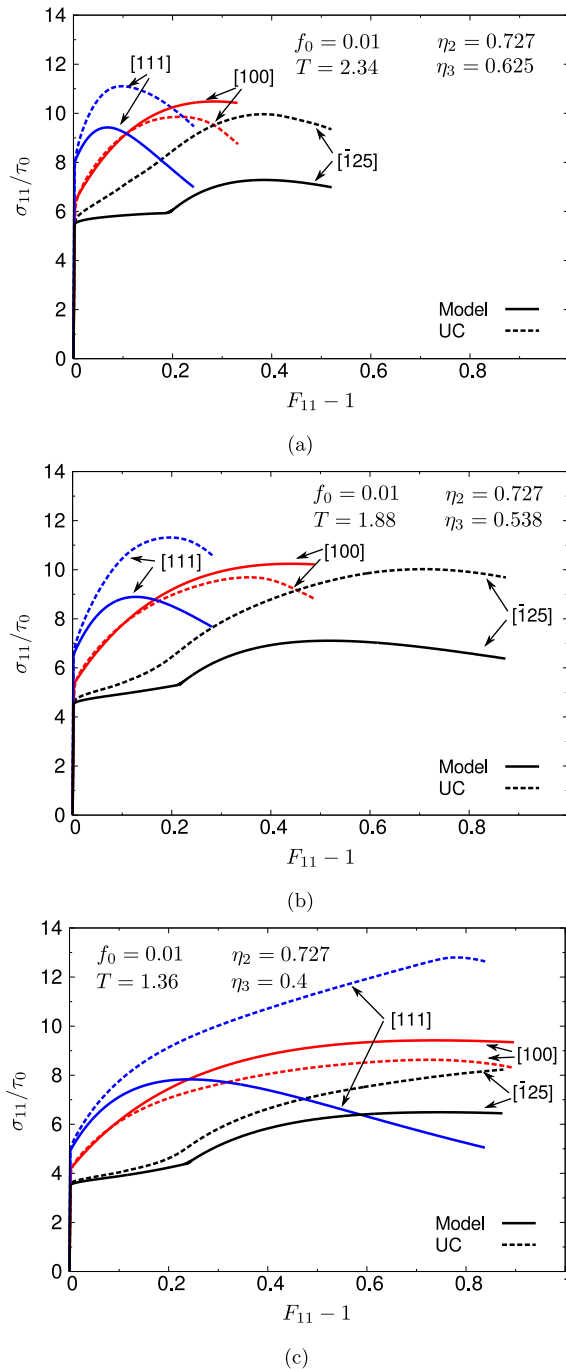


Fig. 18. Assessment of porous single crystal model for non-axisymmetric cases: evolution of normalised macroscopic stress σ_{11}/τ_0 with respect to axial strain $F_{11}-1$ for different crystallographic orientations with initial void volume fraction $f_0 = 0.01$, $\eta_2 = 0.727$ and (a) $\eta_3 = 0.625$, (b) $\eta_3 = 0.538$ and (c) $\eta_3 = 0.4$.

and 16a and at $\eta_2 = \eta_3 = 0.4$ ($T = 3$) in Figs. 14b and 16b. This can probably be explained by the potential influence of the third invariant of the macroscopic stress tensor, which is not yet taken into account in the porous single crystal model.

5.4. Discussion

The comparisons between the porous single crystal model and the unit cell simulations have been presented. The model successfully predicts the hierarchy of the macroscopic stress strain behaviour and the evolution of void volume fraction with

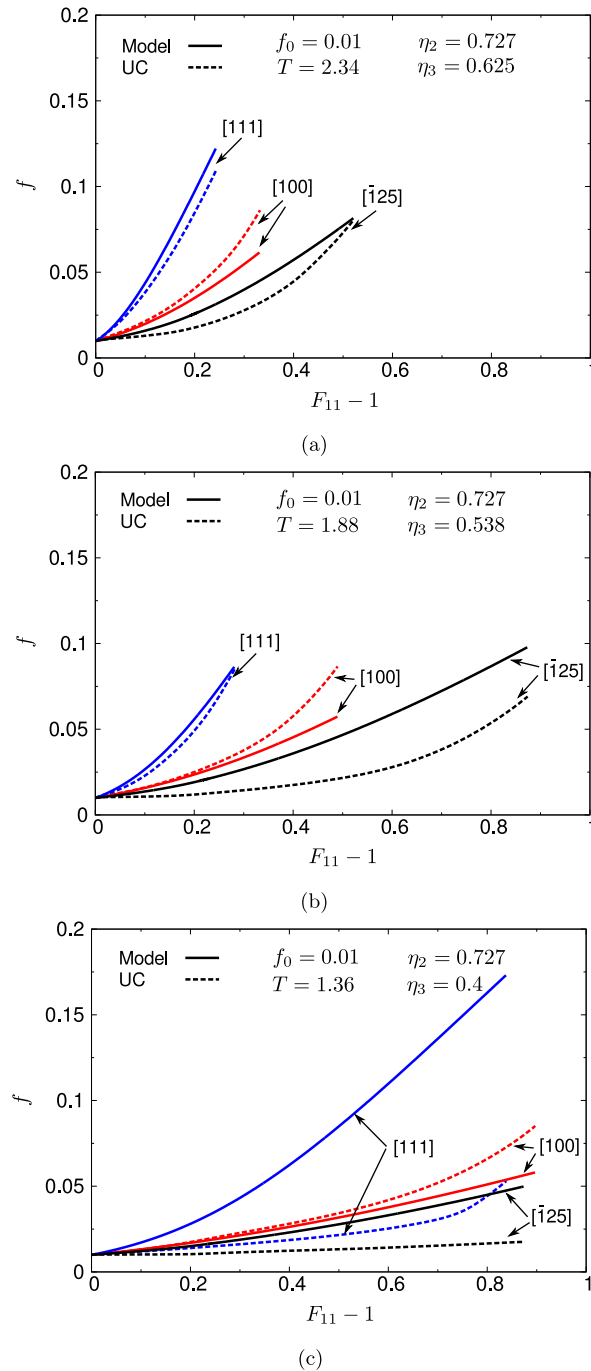


Fig. 19. Assessment of porous single crystal model for non-axisymmetric cases: evolution of void volume fraction f with respect to axial strain $F_{11}-1$ for different crystallographic orientations with initial void volume fraction $f_0 = 0.01$, $\eta_2 = 0.727$ and (a) $\eta_3 = 0.625$, (b) $\eta_3 = 0.538$ and (c) $\eta_3 = 0.4$.

respect to (i) crystallographic orientation, (ii) stress triaxiality, and (iii) initial void volume fraction. An exhaustive list of initial conditions for the simulations was considered. While the model has been verified for most conditions, specific modelling issues have been highlighted.

It has been observed that the porous single crystal model underestimates the strain hardening of the unit cell for the $[\bar{1}25]$ with $f_0 = 0.01$ and $f_0 = 0.05$ at high stress triaxiality $T = 3$. The overall stress strain response of the unit cell simulation and that predicted by the porous model are replotted in Fig. 20 for $f_0 = 0.01$. They are also compared with the stress strain response of the void-free single crystal at the same stress triaxiality. For the void-free (dense) single crystal, plastic deformation begins

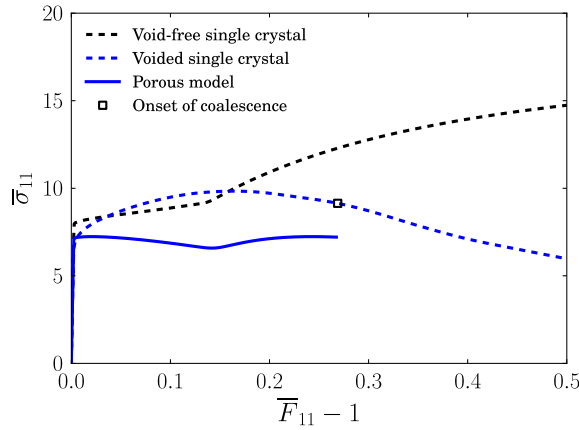


Fig. 20. Stress–strain curves of the void-free and the voided single crystals for the $[\bar{1}25]$ orientation. $T = 3$ and $f_0 = 0.01$.

with a small hardening rate due to the fact that only one slip system is activated. A change of hardening rate occurs when a secondary slip system is activated due to hardening. For the voided single crystal (the unit cell simulation), on the contrary, the plastic part begins with a significant hardening rate, which is related to latent hardening as a result of the multiple slip in the regions near the void as shown in Figs. 8 and 12. To be more precise, an indicator of slip activity is proposed as

$$I = \frac{1}{V} \int \sum_{s=1}^{12} H\left(\frac{|\dot{\gamma}_s^p|}{\dot{F}_{11}}\right) dV, \quad (44)$$

where the Heaviside function $H(x) = 1$ if $x > 0$, else $H(x) = 0$. This quantity indicates the effective number of activated slip systems depending on crystallographic orientation and stress triaxiality in both the model and the unit cell. In Fig. 21, the evolution of the indicator with respect to the strain $F_{11} - 1$ is presented for the $[\bar{1}25]$ orientation with $f_0 = 0.01$. It reveals that the macroscopic porous model predicts single slip pattern for the $[\bar{1}25]$ orientation at $T = 3$. However the factor reaches 4 before void coalescence in the unit cell simulation, which significantly deviates from the single slip pattern. This is confirmed by Figs. 8 and 11. Since fewer activated slip systems are predicted by the porous model, strain hardening is underestimated by the model. The enhancement of latent hardening by the high stress triaxiality observed in the unit cell simulation for the single-slip orientations is difficult to capture in a homogenisation model.

For the $[\bar{1}25]$ orientation with small initial void volume fraction $f_0 = 0.01$ at the low stress triaxiality $T = 1$, the porous model overestimates the void growth rate as compared to the unit cell simulation (see Fig. 16a). The unit cell shows nearly no void growth in terms of void volume fraction. Notice that the $[\bar{1}25]$ orientation corresponds to single slip orientation for a void-free FCC single crystal. For this type of orientation with small initial void volume fraction at low stress triaxiality, the void does not induce significant plastic slip heterogeneity in the single crystal matrix, as shown in Section 4.3. As a result, the

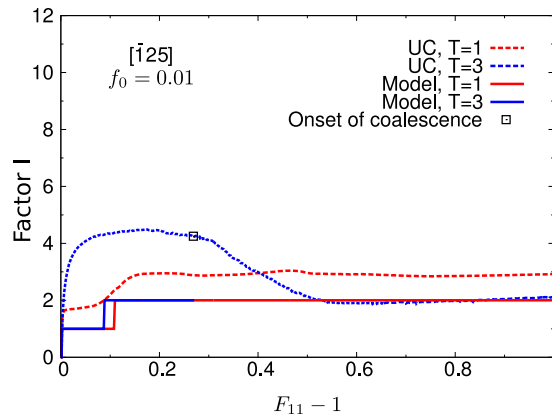


Fig. 21. Comparison between the unit cell simulation and the porous single crystal model: evolution of plastic slip indicator I with respect to axial strain $F_{11} - 1$ for the $[\bar{1}25]$ orientation.

voided single crystal behaves like a void-free single crystal and exhibits a nearly single slip pattern with quasi-incompressible overall behaviour. No void growth is predicted by the unit cell simulation in this case. In contrast, the macroscopic model predicts a weak void growth for this case, due to the term $2q_1f_i\cosh\left\{q_2\sqrt{\frac{3}{20}}\frac{M_m}{\tau_s}\right\}$ in Eq. (21), which is strictly positive even in the case of single slip and, by virtue of normality rule, induces void growth. As the initial void volume fraction increases to $f_0 = 0.05$, the plastic slip heterogeneity introduced by the void becomes significant even at low stress triaxiality. The porous single crystal deviates significantly from single slip and much more slip systems are activated around the void. As a result, in the unit cell simulation, the strain hardening rate is increased and the void growth is accelerated. As the model only considers a single slip situation, it underestimates the strain hardening and the void growth for the $[\bar{1}25]$ orientation with $f_0 = 0.05$ even at low stress triaxiality $T = 1$.

Significant deviations of the model from the reference unit cell computations were also found for the $[111]$ orientation. They are attributed to the strong distortion of the void in that case, see Figs. 8 and 9. This is associated with a significantly larger growth rate than for other orientations. The model qualitatively predicts this higher growth rate.

6. Application to notched single crystal specimens

In this section, the proposed porous single crystal model is used to simulate a small structure so as to show its numerical efficiency. Actual experiments on similar structures will be carried out and compared to simulations. The model is used to simulate the uniaxial tension tests of notched single crystal specimens of Fig. 22. The γ_{cum} and f_i fields near the notch tip are displayed in Fig. 23 for three orientations at the elongation of $\Delta L_0/L_0 = 0.1$. Localisation modes of γ_{cum} and that of f_i are similar for the same orientation. As a result of the symmetry of slip systems, the fields are symmetric for $[100]-[010]-[100]$ and $[111]-[\bar{2}11]-[0\bar{1}1]$, but not for $[\bar{1}25]-[\bar{1}\bar{2}1]-[210]$. The notch is opened in a symmetric manner for $[100]-[010]-[100]$ and $[111]-[\bar{2}11]-[0\bar{1}1]$. In contrast, for $[\bar{1}25]-[\bar{1}\bar{2}1]-[210]$, the notch is opened in one direction more than in the other, due to the inclined localisation band.

Due to plane strain conditions, out-of-plane deformations are restricted in the simulations. They may play an important role in 3D cases, especially for some orientations such as $[\bar{1}25]-[\bar{1}\bar{2}1]-[210]$. In 3D simulations, the notch front may become curved as a result of out-of-plane plastic slip. Despite this, the simulations under plane strain conditions illustrate the capabilities of the model to capture characteristics of notch opening for the three orientations.

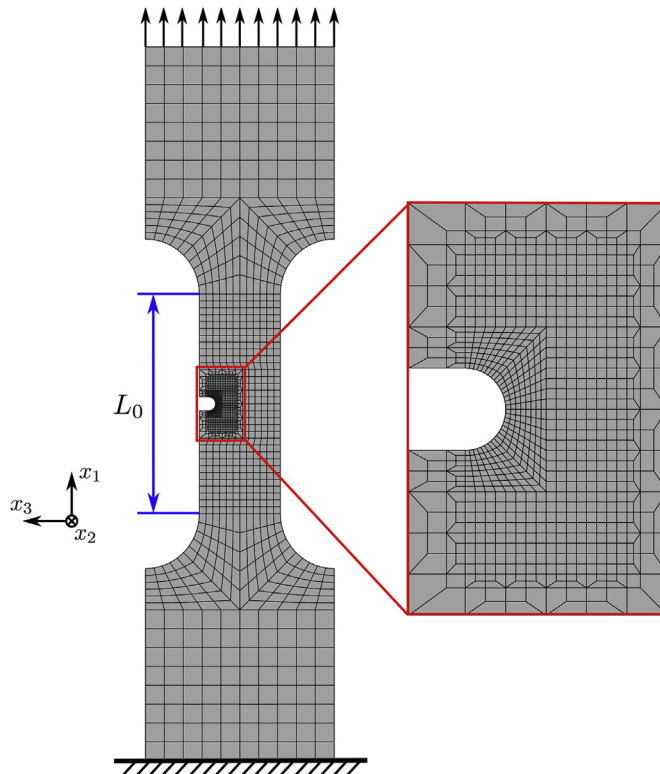


Fig. 22. Finite element mesh of a notched tensile specimen.

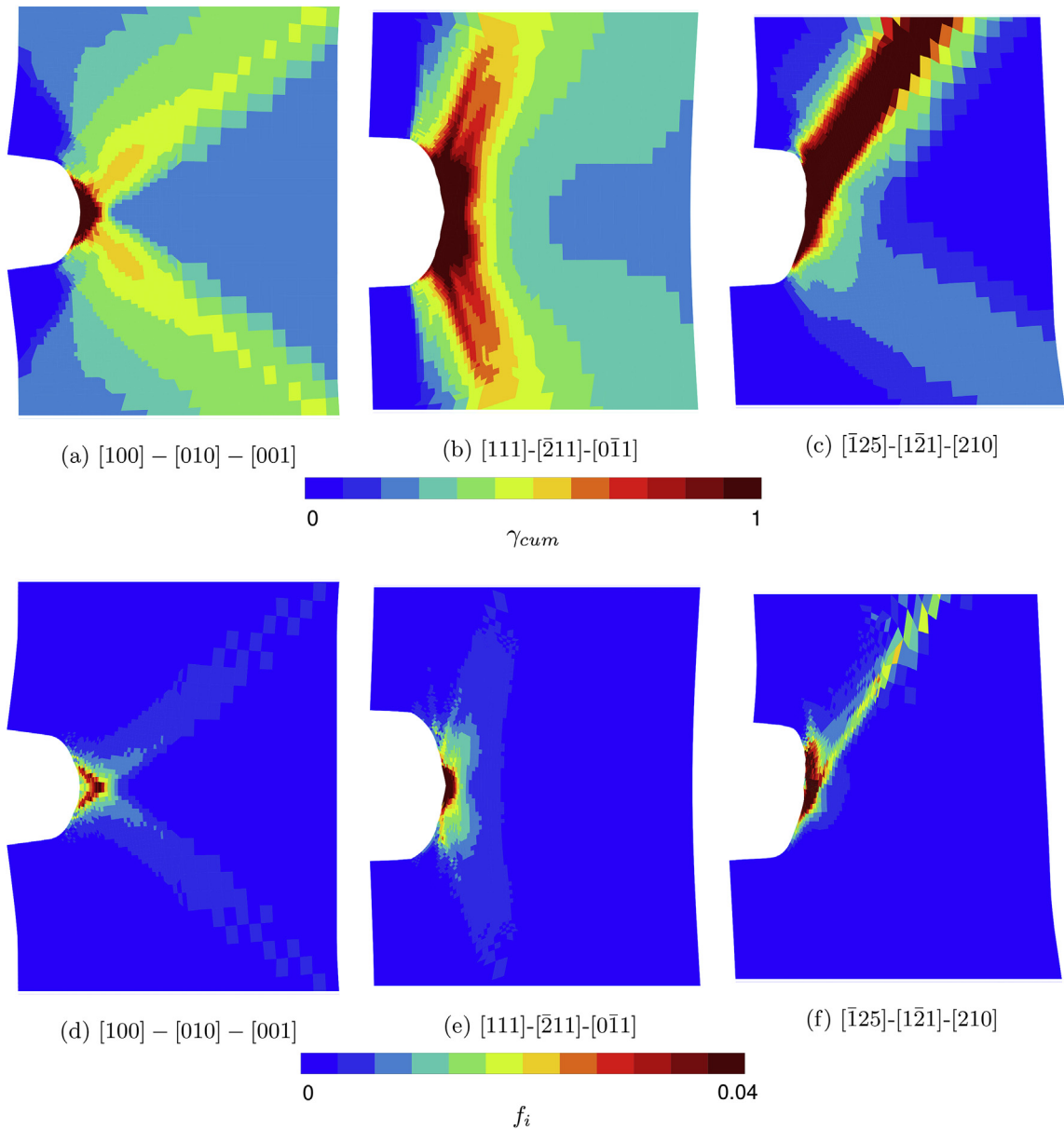


Fig. 23. γ_{cum} fields (a, b and c) and variable f_i fields (d, e and f) around the notch for different orientations.

7. Conclusions

An elastoviscoplastic model has been proposed for porous single crystals undergoing finite deformations for the first time. The proposed model represents a remarkable compromise between description of unit cell behaviour and tractability in the computation of structural components. The effective resolved shear stress defined in the work of Han et al. (2013) at infinitesimal strains is extended to finite strains and the work hardening of the matrix of porous single crystals is incorporated. To the best knowledge of the authors, the proposed macroscopic model is the first model for porous single crystals at finite strains. The model is suitable for FE implementation to carry out structural computations, as shown for uniaxial tension test of notched single crystal specimens.

The model is calibrated from unit cell simulations based on FE periodic homogenisation. Constant stress triaxiality is prescribed with various initial void volume fractions and crystallographic orientations, including the $[210]$ and $[\bar{1}25]$ orientations which exhibit strong anisotropic behaviour. The unit cell simulations show the dependence of overall stress strain response on the crystallographic orientation. The $[111]$ orientation exhibits harder response compared to the other orientations. The void volume fraction evolution also displays an orientation dependence which is more significant at low stress triaxiality. In particular, a quasi absence of void growth is observed for the $[\bar{1}25]$ orientation with small initial void volume

fraction at low stress triaxiality, which leads to quasi-incompressible overall behaviour. In addition, the critical void volume fraction f_c for the onset of coalescence highly depends on crystallographic orientation, while it is almost not influenced by stress triaxiality varying from 1 to 3 for a given crystallographic orientation.

Compared with the unit cell simulations, the porous single crystal model captures the hierarchy of porous single crystal responses with respect to crystal orientation, stress triaxiality and void volume fraction. However, the model does not predict the quasi-incompressible behaviour observed for strongly non-symmetric orientations, e.g., $[\bar{1}25]$, with small initial void volume fraction at low stress triaxiality. The model underestimates the strain hardening for strongly asymmetric orientations with small initial void volume fraction at high stress triaxiality and with large f_0 at all levels of stress triaxiality considered. Improvement of the porous single crystal model may be considered by using the yield criterion of porous single crystals derived from a more appropriate homogenisation approach, such as that of Mbiakop et al. (2015b, 2015a), to define the effective resolved shear stress. Alternative approaches based on admissible stress fields could also be extended to Gurson-like models of void growth in crystals (Chen et al., 2013; Shen et al., 2015). In addition, a new effect was evidenced by our unit cell simulations which is related to enhanced hardening for highly non-symmetric orientations. The effect is due to activation of multislip around the hole and associated latent hardening, whereas the outer matrix remains under single slip conditions. The porous model predicts single slip and does not account for the latent hardening effect, see Fig. 20. It does not seem that other existing porous single crystal models can capture it.

Some other features of porous single crystal behaviour are not included in the model, especially the void size effect, which has been investigated through different approaches (e.g., see Shu (1998), Borg (2007); Borg and Kysar (2007); Fischer and Antretter (2009) for FE unit cell simulations with strain gradient plasticity, see Hussein et al. (2008) and Chang et al. (2015) for DDD simulations, see (Zhao et al., 2009; Krasnikov and Mayer, 2015) for MD and (Carroll et al., 2012; Kadkhodapour et al., 2011) for experimental observations). Future work will focus on this aspect.

In addition, the validation of the porous single crystal model at the polycrystalline scale will also be considered. Based on a second homogenisation procedure, the behaviour of polycrystalline metals containing intragranular voids predicted by the model can be compared with results of experiments and those of simulations with ductile fracture models in the literature (Kabirian and Khan, 2015) and models combining damage and crystal plasticity Kim and Yoon (2015).

Appendix A. Method for imposing constant stress triaxiality and formulation of the boundary value problem of the unit cell simulation

A special truss element has been developed for imposing constant macroscopic Cauchy stress triaxiality under periodic boundary conditions at finite strains.

This element is aligned with the main loading direction, i.e., x_1 -axis. It has only one degree of freedom $\{\hat{F}_{11} - 1\}$ for the node at the far end of the element and nine degrees of freedom $\{\bar{F}_{ij}, i, j = 1, 2, 3\}$ for the node at the near end of the element. It is connected to the unit cell in such a way that the nine degrees of freedom $\{\bar{F}_{ij}, i, j = 1, 2, 3\}$ of the node at the near end correspond to the nine components of the macroscopic deformation gradient of the unit cell, i.e., $\bar{F}_{ij} = \bar{F}_{ij}, i, j = 1, 2, 3$. Consequently, \bar{F}_{ij} will be used instead of \bar{F}_{ij} in the following development for the nine degrees of freedom of the node at the near end of the element.

The element acts as a spring in the main loading direction as follows

$$\hat{S}_{11} = K(\hat{F}_{11} - \bar{F}_{11}), \quad (\text{A.1})$$

with \hat{S}_{11} the first component of the first Piola-Kirchhoff stress tensor and K the element stiffness.

With the macroscopic Cauchy stress $\bar{\sigma}$ taking the form of Eq. (34), the stress triaxiality T imposed over the unit cell follows Eq. (35).

Using Eq. (33), the corresponding macroscopic first Piola-Kirchhoff stress tensor $\bar{\mathcal{S}}$ can be written as

$$\bar{\mathcal{S}} = \bar{J}\bar{\sigma} \cdot \bar{\mathbf{F}}^{-T} = \bar{J}\bar{\sigma}_{11}\bar{\sigma}_0\bar{\mathbf{F}}^{-T}, \quad (\text{A.2})$$

If $\bar{\sigma}_0$ and $\bar{\mathbf{F}}$ are re-written in the matrix form, one has

$$[\bar{\mathcal{S}}_{ij}] = \bar{\sigma}_{11} \begin{bmatrix} F_{22}\bar{F}_{33} - \bar{F}_{23}\bar{F}_{32} & \bar{F}_{23}\bar{F}_{31} - \bar{F}_{21}\bar{F}_{33} & \bar{F}_{21}\bar{F}_{32} - \bar{F}_{22}\bar{F}_{31} \\ \eta_2(\bar{F}_{13}\bar{F}_{32} - \bar{F}_{12}\bar{F}_{33}) & \eta_2(\bar{F}_{11}\bar{F}_{33} - \bar{F}_{13}\bar{F}_{31}) & \eta_2(\bar{F}_{31}\bar{F}_{12} - \bar{F}_{11}\bar{F}_{32}) \\ \eta_3(\bar{F}_{12}\bar{F}_{23} - \bar{F}_{13}\bar{F}_{22}) & \eta_3(\bar{F}_{13}\bar{F}_{21} - \bar{F}_{11}\bar{F}_{23}) & \eta_3(\bar{F}_{11}\bar{F}_{22} - \bar{F}_{12}\bar{F}_{21}) \end{bmatrix}. \quad (\text{A.3})$$

Because of the connection between the unit cell and the truss element at the near end of the element, one can use the Eqs. (A.1) and (A.3) and obtain

$$\hat{S}_{11} = \bar{S}_{11}. \quad (\text{A.4})$$

Thus, one can get

$$\bar{\sigma}_{11} = \frac{K(\hat{F}_{11} - \bar{F}_{11})}{\bar{F}_{22}\bar{F}_{33} - \bar{F}_{23}\bar{F}_{32}}. \quad (\text{A.5})$$

As a result, the macroscopic first Piola-Kirchhoff stress applied over the unit cell via the truss element is equal to

$$[\bar{S}_{ij}] = \frac{K(\hat{F}_{11} - \bar{F}_{11})}{\bar{F}_{22}\bar{F}_{33} - \bar{F}_{23}\bar{F}_{32}} \begin{bmatrix} \bar{F}_{22}\bar{F}_{33} - \bar{F}_{23}\bar{F}_{32} & \bar{F}_{23}\bar{F}_{31} - \bar{F}_{21}\bar{F}_{33} & \bar{F}_{21}\bar{F}_{32} - \bar{F}_{22}\bar{F}_{31} \\ \eta_2(\bar{F}_{13}\bar{F}_{32} - \bar{F}_{12}\bar{F}_{33}) & \eta_2(\bar{F}_{11}\bar{F}_{33} - \bar{F}_{13}\bar{F}_{31}) & \eta_2(\bar{F}_{31}\bar{F}_{12} - \bar{F}_{11}\bar{F}_{32}) \\ \eta_3(\bar{F}_{12}\bar{F}_{23} - \bar{F}_{13}\bar{F}_{22}) & \eta_3(\bar{F}_{13}\bar{F}_{21} - \bar{F}_{11}\bar{F}_{23}) & \eta_3(\bar{F}_{11}\bar{F}_{22} - \bar{F}_{12}\bar{F}_{21}) \end{bmatrix}, \quad (\text{A.6})$$

such that constant macroscopic Cauchy stress triaxiality T is imposed as Eq. (35).

Finally, the boundary value problem, considered in unit cell simulations with prescribed stress triaxiality and periodic boundary conditions, is to search the periodic fluctuation vector $\underline{\mathbf{v}}$ when imposing \hat{F}_{11} such that

- the balance of momentum:

$$\text{div } \underline{\underline{\sigma}} = \underline{\underline{0}}, \forall \underline{\underline{\mathbf{x}}} \in \Omega^{tot} \quad (\text{A.7})$$

- and the boundary conditions:

– Periodicity:

$$\underline{\underline{\mathbf{u}}} = \bar{\underline{\underline{\mathbf{F}}}} \cdot \underline{\underline{\mathbf{x}}} + \underline{\underline{\mathbf{v}}}, \forall \underline{\underline{\mathbf{x}}} \in \Omega^{tot} \quad (\text{A.8})$$

– Rotation restriction:

$$\bar{F}_{12} = \bar{F}_{21}, \bar{F}_{23} = \bar{F}_{32}, \bar{F}_{31} = \bar{F}_{13} \quad (\text{A.9})$$

– Rigid translation restriction

$$\underline{\underline{\mathbf{u}}}(\underline{\underline{\mathbf{X}}}_n) = \underline{\underline{0}}, \underline{\underline{\mathbf{X}}}_n \text{ is the coordinates of a chosen node of the unit cell} \quad (\text{A.10})$$

– Loading via the truss element

$$\bar{S}_{11} = K(\hat{F}_{11} - \bar{F}_{11}) \quad (\text{A.11})$$

– Constant macroscopic Cauchy stress triaxiality

$$\bar{\sigma}_{12} = \bar{\sigma}_{23} = \bar{\sigma}_{31} = 0 \text{ and } \bar{\sigma}_{22} = \eta_2 \bar{\sigma}_{11}, \bar{\sigma}_{33} = \eta_3 \bar{\sigma}_{11} \quad (\text{A.12})$$

are fulfilled.

References

- Benzerga, A., Leblond, J.B., 2010. Ductile fracture by void growth to coalescence. *Adv. Appl. Mech.* 44, 169–305.
- Besson, J., 2009. Damage of ductile materials deforming under multiple plastic or viscoplastic mechanisms. *Int. J. Plast.* 25, 2204–2221.
- Besson, J., 2010. Continuum models of ductile fracture: a review. *Int. J. Damage Mech.* 19, 3–52. <http://ijd.sagepub.com/content/19/1/3.full.pdf+html>.
- Besson, J., Foerch, R., 1998. Object-oriented programming applied to the finite element method part I. general concepts. *Rev. Eur. des Iments* 7, 535–566.
- Borg, U., 2007. Strain gradient crystal plasticity effects on flow localization. *Int. J. Plast.* 23, 1400–1416.
- Borg, U., Kysar, J.W., 2007. Strain gradient crystal plasticity analysis of a single crystal containing a cylindrical void. *Int. J. Solids Struct.* 44, 6382–6397.

- Carroll, J.D., Brewer, L.N., Battaile, C.C., Boyce, B.L., Emery, J.M., 2012. The effect of grain size on local deformation near a void-like stress concentration. *Int. J. Plast.* 39, 46–60.
- Chang, H.J., Segurado, J., Llorca, J., 2015. Three-dimensional dislocation dynamics analysis of size effects on void growth. *Scr. Mater.* 95, 11–14.
- Chen, L., de Saxcé, G., Kondo, D., 2013. A stress-based variational model for ductile porous materials. *Int. J. Plast.* 55, 133–151.
- Crépin, J., Bretheau, T., Caldemaison, D., 1996. Cavity growth and rupture of β -treated zirconium: a crystallographic model. *Acta Mater.* 44, 4927–4935.
- Danas, K., Aravas, N., 2012. Numerical modeling of elasto-plastic porous materials with void shape effects at finite deformations. *Compos. Part B Eng.* 43, 2544–2559 (Homogenization and Micromechanics of Smart and Multifunctional Materials).
- DeBotton, G., Castaneda, P.P., 1995. Variational estimates for the creep behaviour of polycrystals. *Proc. Royal Society London Math. Phys. Eng. Sci.* 448, 121–142.
- Farrissey, L., Ludwig, M., McHugh, P., Schmauder, S., 2000. An atomistic study of void growth in single crystalline copper. *Comput. Mater. Sci.* 18, 102–117.
- Fischer, F.D., Antretter, T., 2009. Deformation, stress state and thermodynamic force for a growing void in an elastic-plastic material. *Int. J. Plast.* 25, 1819–1832.
- Fritzen, F., Forest, S., Böhlke, T., Kondo, D., Kanit, T., 2012. Computational homogenization of elasto-plastic porous metals. *Int. J. Plast.* 29, 102–119.
- Gan, Y.X., Kysar, J.W., Morse, T.L., 2006. Cylindrical void in a rigid-ideally plastic single crystal II: experiments and simulations. *Int. J. Plast.* 22, 39–72.
- Ha, S., Kim, K., 2010. Void growth and coalescence in F.C.C. single crystals. *Int. J. Mech. Sci.* 52, 863–873.
- Han, X., 2012. Modélisation de la fragilisation due au gonflement dans les aciers inoxydables austénitiques irradiés. Ph.D. thesis. Mines ParisTech.
- Han, X., Besson, J., Forest, S., Tanguy, B., Bugat, S., 2013. A yield function for single crystals containing voids. *Int. J. Solids Struct.* 50, 2115–2131.
- Hussein, M., Borg, U., Niordson, C., Deshpande, V., 2008. Plasticity size effects in voided crystals. *J. Mech. Phys. Solids* 56, 114–131.
- Kabirian, F., Khan, A.S., 2015. Anisotropic yield criteria in σ - τ stress space for materials with yield asymmetry. *Int. J. Plast.* 67–68, 116–126.
- Kadkhodapour, J., Butz, A., Ziaei-Rad, S., Schmauder, S., 2011. A micro mechanical study on failure initiation of dual phase steels under tension using single crystal plasticity model. *Int. J. Plast.* 27, 1103–1125.
- Kim, J.B., Yoon, J.W., 2015. Necking behavior of AA 6022-T4 based on the crystal plasticity and damage models. *Int. J. Plast.* 73, 3–23.
- Koplik, J., Needleman, A., 1988. Void growth and coalescence in porous plastic solids. *Int. J. Solids Struct.* 24, 835–853.
- Krasnikov, V.S., Mayer, A.E., 2015. Plasticity driven growth of nanovoids and strength of aluminum at high rate tension: molecular dynamics simulations and continuum modeling. *Int. J. Plast.* 74, 75–91.
- Kubin, L., Devincere, B., Hoc, T., 2008. Modeling dislocation storage rates and mean free paths in face-centered cubic crystals. *Acta Mater.* 56, 6040–6049.
- Kysar, J.W., Gan, Y.X., Mendez-Arzuza, G., 2005. Cylindrical void in a rigid-ideally plastic single crystal. part I: anisotropic slip line theory solution for face-centered cubic crystals. *Int. J. Plast.* 21, 1481–1520.
- Lebensohn, R., Escobedo, J., Cerreta, E., Dennis-Koller, D., Bronkhorst, C., Bingert, J., 2013. Modeling void growth in polycrystalline materials. *Acta Mater.* 61, 6918–6932.
- Mandel, J., 1973. Equations constitutives et directeurs dans les milieux plastiques et viscoplastiques. *Int. J. Solids Struct.* 9, 725–740.
- Mbiakop, A., Constantinescu, A., Danas, K., 2015a. An analytical model for porous single crystals with ellipsoidal voids. *J. Mech. Phys. Solids* 84, 436–467.
- Mbiakop, A., Constantinescu, A., Danas, K., 2015b. A model for porous single crystals with cylindrical voids of elliptical cross-section. *Int. J. Solids Struct.* 6465, 100–119.
- O'Regan, T.L., Quinn, D.F., Howe, M.A., McHugh, P.E., 1997. Void growth simulations in single crystals. *Comput. Mech.* 20, 115–121.
- Orsini, V., Zikry, M., 2001. Void growth and interaction in crystalline materials. *Int. J. Plast.* 17, 1393–1417.
- Paux, J., Morin, L., Brenner, R., Kondo, D., 2015. An approximate yield criterion for porous single crystals. *Eur. J. Mech. A/Solids* 51, 1–10.
- Sabnis, P., Mazière, M., Forest, S., Arakere, N.K., Ebrahimi, F., 2012. Effect of secondary orientation on notch-tip plasticity in superalloy single crystals. *Int. J. Plast.* 28, 102–123.
- Sabnis, P.A., Forest, S., Arakere, N.K., Yastrebov, V., 2013. Crystal plasticity analysis of cylindrical indentation on a Ni-base single crystal superalloy. *Int. J. Plast.* 51, 200–213.
- Schmid, V.E., Boas, W., 1935. *Kristallplastizität*. Verlag Julius Springer, Berlin.
- Segurado, J., Llorca, J., 2010. Discrete dislocation dynamics analysis of the effect of lattice orientation on void growth in single crystals. *Int. J. Plast.* 26, 806–819.
- Shanthraj, P., Zikry, M.A., 2012. Dislocation-density mechanisms for void interactions in crystalline materials. *Int. J. Plast.* 34, 154–163.
- Shen, W.Q., Oueslati, A., de Saxcé, G., 2015. Macroscopic criterion for ductile porous materials based on a statically admissible microscopic stress field. *Int. J. Plast.* 70, 60–76.
- Shu, J.Y., 1998. Scale-dependent deformation of porous single crystals. *Int. J. Plast.* 14, 1085–1107.
- Srivastava, A., Gopagoni, S., Needleman, A., Seetharaman, V., Staroselsky, A., Banerjee, R., 2012. Effect of specimen thickness on the creep response of a Ni-based single-crystal superalloy. *Acta Mater.* 60, 5697–5711.
- Srivastava, A., Needleman, A., 2013. Void growth versus void collapse in a creeping single crystal. *J. Mech. Phys. Solids* 61, 1169–1184.
- Srivastava, A., Needleman, A., 2015. Effect of crystal orientation on porosity evolution in a creeping single crystal. *Mech. Mater.* 90, 10–29 (Proceedings of the IUTAM Symposium on Micromechanics of Defects in Solids).
- Yerra, S., Tekoglu, C., Scheyvaerts, F., Delannay, L., Houtte, P.V., Pardoën, T., 2010. Void growth and coalescence in single crystals. *Int. J. Solids Struct.* 47, 1016–1029.
- Zhao, K., Chen, C., Shen, Y., Lu, T., 2009. Molecular dynamics study on the nano-void growth in face-centered cubic single crystal copper. *Comput. Mater. Sci.* 46, 749–754. Proceedings of the 18th International Workshop on Computational Mechanics of Materials IWCMM-18.